



Quasi-static Confined Uniaxial Compaction of Granular Alumina and Boron Carbide Observing the Particle Size Effects

Journal:	<i>Journal of the American Ceramic Society</i>
Manuscript ID	JACERS-44392.R2
Manuscript Type:	Research Article
Date Submitted by the Author:	10-Oct-2019
Complete List of Authors:	Nicewicz, Piotr; University of Alberta, Mechanical Engineering Peciar, Peter Macho, Oliver Sano, Tomoko Hogan, James; The Johns Hopkins University, Mechanical Engineering
Keywords:	alumina, boron carbide, compacts/compaction, densification, mechanical properties
Author-supplied Keyword: If there is one additional keyword you would like to include that was not on the list, please add it below::	

SCHOLARONE™
Manuscripts

Quasi-static Confined Uniaxial Compaction of Granular Alumina and Boron Carbide Observing the Particle Size Effects

P. Nicewicz^{a,1}, P. Peciar^c, O. Macho^c, T. Sano^b, J.D. Hogan^{a,2,*}

^a*Department of Mechanical Engineering, University of Alberta, Edmonton AB, T6G2R3*

^b*Weapons and Materials Research Directorate, U.S. Army Research Laboratory, Aberdeen Proving Ground, MD 21005, USA*

^c*Institute of Process Engineering, Faculty of Mechanical Engineering, Slovak University of Technology in Bratislava, Námetie Slobody 17, 812 31 Bratislava, Slovakia*

Abstract

The quasi-static uniaxial confined compaction of granular alumina and boron carbide was studied, observing the triaxial stress effects of the materials as a function of increasing particle size. The average particle sizes studied for granular alumina were: $170 \pm 63 \mu\text{m}$, $230 \pm 55 \mu\text{m}$, $330 \pm 67 \mu\text{m}$, and $450 \pm 83 \mu\text{m}$. The average particle size studied for granular boron carbide were: $170 \pm 40 \mu\text{m}$, $190 \pm 34 \mu\text{m}$, $320 \pm 59 \mu\text{m}$, and $470 \pm 90 \mu\text{m}$. The material response in hydro-static pressure as a function of porosity, the bulk modulus as a function of hydro-static pressure, and the transmission ratio as a function of applied load was captured for increasing particle size. Our observations for alumina revealed: increasing particle size resulted in an increase in strength for a fixed porosity, the bulking in this material did not show clear particle-size dependent trends, and the transmission ratio showed increasing behaviour where larger particles transmitted more load. Conversely, for granular

*Corresponding author

¹Email address: pnicewic@ualberta.ca

²Email address: jdhogan@ualberta.ca

Preprint submitted to Journal of the American Ceramic Society

October 22, 2019

1
2
3
4
5 boron carbide: the path of crushing out porosity decreased with increasing particle
6 size, the change in bulking of the material increased with increasing particle size,
7 and no clear particle-size dependent trends were observed when looking at the
8 transmission ratio during the experiment. Post-experiment SEM analysis revealed
9 that alumina powder fragmented from elongated shapes to block-like structures,
10 while the boron carbide powder appeared more circular before the experiments and
11 fragmented into smaller comminuted pieces. The paper discusses the implication
12 of the work in the context of the limited experimental data in the field and the
13 modelling of granular advanced ceramics behaviour.
14
15
16
17
18
19
20

21 *Keywords:* granular, confined, uniaxial compaction, quasi-static, ceramics,
22 fragmentation
23
24

25 26 27 **1. Introduction**

28
29 Ceramic materials have been used in many different applications due to their su-
30 perior material properties. Inherent in the response of ceramics, and brittle materials
31 in general, is their ability to undergo fracture and fragmentation. These behaviours
32 have been noted for rocks in the planetary science applications describing asteroid
33 fragmentation [1], geological research in optimizing blasting of mines [2], and blast
34 mitigation in the defence industry [3]. Of particular interest in this study, is the use
35 of ceramics in protection applications [3–5], where our ability to control fracture and
36 fragmentation behaviours is believed to be central to improving their performance.
37
38
39
40
41
42
43

44 Ceramics emerged in ballistic protection applications around the 1960's [6]. They
45 have been used to mitigate various threats ranging from high pressure blasts to pro-
46 jectile and fragment penetration [3, 4, 7, 8]. Due to the superior strength-to-weight
47 ratio and impact resistance, advanced ceramics have been used in the protecting ve-
48
49
50
51
52

1
2
3
4
5 hicles and personnel in combat situations ever since. Accompanying research on the
6 development of advanced protection applications have included, for example, study-
7 ing multi-hit capabilities of armour protection [4], the dwell-penetration relationship
8 in projectile penetration [9], and fragmentation behaviour on projectile erosion and
9 energy dissipation [10]. Advanced ceramics such as alumina (Al_2O_3), silicon car-
10 bide (SiC), and boron carbide (B_4C) have been researched in literature due to their
11 high hardness, and low density, which are key parameters to making high energy
12 dissipation, but lightweight defence materials [11, 12].
13
14
15
16
17
18

19
20 In many studies, fragmentation and comminution has been noted to be impor-
21 tant in the ballistic performance of advanced ceramics [11–15]. [16] was one of the
22 first researchers to couple physical and statistical theories of fragmentation. Later
23 work by [17] noted that fragmentation occurs in three stages: crack nucleation, crack
24 growth, and crack coalescence where they successfully related comminution sizes to
25 mechanical properties and loading rates. Other work by [18] observed distinct frag-
26 mentation regimes during the impact of boron carbide. Relatively smaller fragments
27 ($<100\ \mu\text{m}$) appeared to be micro-structure dependent and arose from coalescence
28 of fractures, while relatively larger fragments ($>100\ \mu\text{m}$) were more so dependent on
29 specific structural mechanisms (buckling of columns) rather than material. Likewise,
30 fragmentation was underlined by [12] where they concluded that penetration resis-
31 tance is governed by compressive stiffness, hardness, pulverization characteristics,
32 frictional flow of fragments, and fragment abrasiveness (i.e. particle geometry) dur-
33 ing impact. With comminution happening as a primary material failure mechanism,
34 the incentive of studying ceramics in a granular state increase.
35
36
37
38
39
40
41
42
43
44
45

46
47 The study of fragmentation and fracture leads us to granular behaviour, failure,
48 and mechanical properties of advanced ceramics. Granular advanced ceramics have
49 been investigated before, [19–22], nonetheless, it is limited, likely as a result of the
50
51
52

1
2
3
4
5 natural material hardness making it difficult to conduct experiments. Modelling ef-
6
7
8
9
10
11
12
13
14
15
16
17
18
19
20
21
22
23
24
25
26
27
28
29
30
31
32
33
34
35
36
37
38
39
40
41
42
43
44
45
46
47
48
49
50
51
52
53
54
55
56
57
58
59
60

natural material hardness making it difficult to conduct experiments. Modelling efforts simulating the behaviour of granulated advanced ceramics has also been limited [23], with the majority of the literature on experimentation and modelling the behaviour of geological materials [24–29]. In their study, [30] in their simulation study, demonstrated the importance of the behaviour of the damaged and granular forms of advanced ceramics on penetration resistance and characterizing stress by observing that particle size distribution better explained such behaviour. The damaged and granular ceramic should not be discounted post-impact due to a significant amount of residual stiffness that continues to contribute to the overall response of the material. Motivated by these past works, this current paper seeks to investigate the failure and fragmentation of granular advanced ceramics contributing to a limited set of data in the open literature.

During impact, the material responds through particle breakage, fragment rearrangement causing compaction, and frictional interactions. In order to better understand the behaviour of advanced ceramics for defence applications, the shortcomings of powder flowability, particle variability, and particle performance relating to granular material stress must be addressed and understood [31]. Overall, the importance of fracture and fragmentation on the impact performance of ceramics has been well documented in the literature [13, 17, 32–34]. Building on these past works, this paper explores the behaviour of granular alumina and boron carbide with an emphasis on the effect of particle size and shape on hydro-static pressure and variability in stiffness, bulk modulus, and frictional effects. A quasi-static experimental technique (strain rates of 10^{-3}s^{-1}) is used to evaluate the triaxial response as a function of the granular ceramic's particle size. The quasi-static static confined compaction behaviour is chosen as starting point for better understanding the impact fragmentation problem, recognizing that high rate behaviour [17, 18, 20] is also important. SEM

1
2
3
4
5 imaging was used to investigate failure, fracture, and fragmentation mechanisms be-
6 fore and after experiments. Particle size measurements are performed before and af-
7 ter experiments to probe the degree of comminution. In the Discussion, we highlight
8 the work in the context of existing limited data in the literature and for modelling
9 implications.
10
11
12
13
14

15 *1.1. Experimental Techniques*

16 *1.2. Material*

17 *1.2.1. Composition and Geometry*

18
19 Alumina and boron carbide powder was used in the experiment and was pur-
20 chased from Panadyne Inc, Montgomeryville, Pennsylvania. The average particle
21 sizes for Al_2O_3 used for the uniaxial compaction were four different size ranges: 1.
22 $170 \pm 63 \mu\text{m}$, 2. $230 \pm 55 \mu\text{m}$, 3. $330 \pm 67 \mu\text{m}$, and 4. $450 \pm 83 \mu\text{m}$. Likewise, the
23 average particle size range for B_4C consisted of: 1. $170 \pm 40 \mu\text{m}$, 2. $190 \pm 34 \mu\text{m}$, 3.
24 $320 \pm 59 \mu\text{m}$, and 4. $470 \pm 90 \mu\text{m}$. These particles sizes were determined using the
25 PartAn 3D Dynamic Image Analyzer, and the sampling methods and other particle
26 characteristics are subsequently discussed. The materials used in the experiments
27 are classified as coarse particles based on the NIST Recommended Particle Guide -
28 The use of Nomenclatures in Dispersion Science and Technology [35]
29
30
31
32
33
34
35
36
37
38

39 To study the particle shape, size features before experiments, and the failure after
40 experiments of Al_2O_3 , the Zeiss EVO MA10 Scanning Electron Microscope (SEM)
41 was used and the samples were coated with gold/palladium at 4 nm to improve the
42 quality of the images taken. Shown in Figure 1(a) is an SEM image of Al_2O_3 powder
43 ($170 \pm 63 \mu\text{m}$) before the experiment. The overall geometry appears to be elongated
44 with sharp edges with and the average aspect ratio (width to height) ranges from 0.2
45 to 0.7. There is also some minor porosity in the fragments. These shape and porosity
46
47
48
49
50
51
52

1
2
3
4
5 features are consistent across all fragment sizes for alumina used in this study. These
6 elongated alumina particles were chosen for the compression experiment because as
7 noted before by [11] during ballistic impact, brittle ceramic materials fracture into
8 elongated shard fragments.
9
10

11
12 For boron carbide, the particle geometry and structure of the powder was imaged
13 using a JSM-IT300 SEM. Those samples were coated with palladium to improve the
14 quality of the images. Shown in Figure 2(a) is an SEM image of the boron carbide
15 fragments for sizes of $170 \pm 40 \mu\text{m}$. The particles have aspect ratios close to 1, with
16 some appearing spherical and other appearing block-like in nature. There is some
17 minor porosity in the fragments. Next, the fragment size range of $320 \pm 59 \mu\text{m}$ for
18 boron carbide is shown in Figure 2(b). Here, the larger fragments are also mostly
19 near-spherical, but with fewer block like fragments shown than for the smaller sizes.
20 The aspect ratio's of the particles were documented and are summarized in Table 1
21 for alumina and Table 2 for boron carbide. The granular alumina and boron carbide
22 were analyzed separately and the difference in geometries was unique. The other
23 images in Figure 1 and Figure 2 are discussed later when we investigate material
24 failure post experiment.
25
26
27
28
29
30
31
32
33
34
35
36

37 *1.2.2. Particle Distribution*

38
39 Four different size ranges were sieved, microscopically analyzed, and tested to
40 observe the effects of mean particle diameter, (μm), and shape, on hydro-static
41 pressure, P (MPa), as a function of porosity, ϕ (%), for alumina and boron carbide.
42 The alumina and boron carbide were initially sieved, and particle size and shape
43 were investigated using the PartAn 3D Dynamic Image Analyzer to analyze the
44 particles before the experiments. The particle size distribution was analyzed on the
45 basis of dynamic image analysis where the area equivalent diameter, D_a (μm), was
46
47
48
49
50
51
52

considered. This parameter is relevant when determining the distribution of the bulk sample used in the experiment and is the default principle used by the PartAn analyzer. To calculate this parameter the following equation is used:

$$Da = \left(\frac{4A}{\pi} \right)^{\frac{1}{2}} \quad (1)$$

were A (μm^2) is the area of the projected image. The same sieves and machine were used to analyze and test B_4C powder. The cumulative distribution plot pre and post compression of the particle diameter for alumina and boron carbide is illustrated in Figure 10 and Figure 11, respectively. The mean and standard deviation were documented for each particle size, and these results are summarized in Table 1 for alumina and Table 2 for boron carbide. Three samples of each material were tested and each specimen was sampled following principal sampling techniques for granular material outlined by [36]. To evaluate the relative variability of the powder, the span was calculated for each sample as was similarly used by [37] where the equation takes into account the tenth (D_{10}), fiftieth (D_{50}), and ninetieth percentile (D_{90}):

$$\Delta = \frac{D_{90} - D_{10}}{D_{50}} \quad (2)$$

After the experiments were performed, the particle sizes were characterized using a Malvern Instruments Morphologi G3. The Morphologi G3 is used instead of the Microtrac PartAn 3-D microscope because the Morphologi G3 is capable of measuring to smaller particle sizes (~ 1 micron compared to ~ 22 microns for the PartAn 3-D). Regardless, in both measurements, the longest spanning dimensions is taken as the size of the particle.

1.3. Confined Uniaxial Quasi-static Compaction Experiments

1.3.1. Configuration

Illustrated in Figure 3 is a schematic of the experimental apparatus used to conduct uniaxial confined compaction experiments on the granular material. The top and bottom punch are fabricated from O2 tool steel so that the high stiffness would transfer a maximum load through the specimen. The punches are used to press together the granular material. The top and bottom punches are designed around the accessibility of the Kistler electro-mechanical press machine used in this study. The crucible was made out of O2 tool steel with an inner diameter of 6 mm and outer diameter of 22.2 mm. The inner diameter was machined with a tight tolerance to seal in the granular material during compaction. The force was measured from the top and bottom axial load cell, depicted in Figure 3. To calculate the radial stress in the sample, the radial displacement deflected the radial load cell that outputs a force magnitude. The diameter of the radial rod was 3 mm. Attached to the press was a linear variable differential transformer (LVDT, not shown in Figure 3) so that relative displacement could be recorded to track the initial and final volume of the specimen. The press machine outputted the applied load from the top, at a rate of 0.5 mm s^{-1} , placing the specimen in a quasi-static strain state.

In order to limit the wall frictional effects occurring during confined compaction, it is critical to maintain an aspect ratio of height to width of < 1 for the poured powder according to [38]. The granular material was poured into the crucible void and a final aspect ratio of 0.59 was achieved during compaction. The obtained void volume was not the same for all samples because of the varying particle size and the uncertainty in initial volume was $209 \pm 13 \text{ mm}^3$ for Al_2O_3 , and $209 \pm 7 \text{ mm}^3$ for B_4C . The differences are as a result of the nature of small amounts of granular material

1
2
3
4
5 and the geometrical constraints of the void size making it difficult to obtain identical
6 amounts of material. Shown in Table 3 (for alumina) and Table 4 (for boron carbide)
7 are the sample specifications for each test presented here, including mean diameter
8 with standard deviation, initial mass, initial volume, initial density, final density,
9 initial porosity, and final porosity after the experiment.
10
11
12
13

14 To perform the testing, the material was carefully poured into the void and the
15 top punch was rested up on the sample. The top hydraulic arm was then lowered
16 to compress the granular material to a maximum force of 50 kN. The LVDT was
17 secured to the top arm, so that the relative compaction depth could be measured.
18 Next, we outline the theory used to interpret the measurements.
19
20
21
22

23 24 *1.3.2. Theory*

25 To better understand the triaxial response of the granular material during quasi-
26 static uniaxial compression, we investigate the relationship between the hydro-static
27 pressure and porosity by tracking the axial stress, radial stress, and relative density
28 in the confined crucible. First, we track the reduction in porosity of our test samples
29 through measurements of initial mass m (kg), initial packing porosity ϕ_i (%), and
30 the cross-head displacement δ (mm) of the top punch that is used to compress the
31 samples. The mass of the initial granular sample is measured by a digital scale with
32 the precision of 0.0001 g, and values for each experiment are listed in Table 1 (for
33 alumina) and Table 2 (for boron carbide). The sample size was volume controlled
34 with a limiting void volume of 209 mm³. Throughout the compression experiment,
35 the change in displacement, δ (mm), is related to change in volume, ΔV (m³):
36
37
38
39
40
41
42
43
44
45

$$46 \quad \Delta V = A_0 \delta \quad (3)$$

47 where A_0 is the cross-section area of the sample (m²) which corresponds to the cross-
48
49
50
51

sectional area of the void and δ is the relative axial displacement during compression (m). The cross-sectional area of the void corresponds to the cross-sectional area of the sample tested. From there, we calculate the apparent density ρ (kg m^{-3}), as it evolves during compaction:

$$\rho = \frac{m}{V_0 - \Delta V} \quad (4)$$

where m is the mass of the specimen (kg), and V_0 is the initial specimen volume (m^3). The evolving porosity is calculated by normalizing the specimen density with the solid bulk density:

$$\phi = 1 - \frac{\rho}{\rho_s} \quad (5)$$

where ϕ is the porosity fraction (unit less) and ρ_s is the bulk solid density (kg m^{-3}). For Al_2O_3 and B_4C , the bulk density is taken as 3987 kg m^{-3} and 2520 kg m^{-3} , respectively.

Next, the hydro-static pressure is calculated by measuring the difference in axial stress, P_z (MPa), from the top and bottom load cell and the radial stress, P_r (MPa), from the perpendicular mounted load cell. Refer to the schematic in Figure 3 for orientation. The equation for hydro-static stress, P (MPa), can be written as:

$$P = \frac{1}{3} (P_z + 2P_r) \quad (6)$$

To calculate the axial stress, P_z , we divide the difference in axial force experienced by the sample, F_z (N), and the cross-sectional area of the void A_0 (m^2), assuming that the area does not change during compression:

$$P_z = \frac{F_z}{A_0} \quad (7)$$

As mentioned before, F_z was computed by subtracting the axial forces outputted by the top and bottom load cell, respectively, so that we can account for the wall friction effects introduced during compaction.

To determine the radial stress, the radial force was transferred from the material by a thin shaft that was located at the centre of the uncompressed specimen (see Figure 3). As compaction commenced, the thin shaft was pressed against the load cell mounted perpendicular to the apparatus, which recorded the force. Using (8), the radial stress was calculated:

$$P_r = \frac{F_r}{A_r} \quad (8)$$

where F_r is the radial force (N) and A_r is the cross-sectional area, (m^2). By machining the moving pieces with high tolerances, the contact friction between the shaft and hole can be neglected.

Once the hydro-static pressure and stresses are known, we can also investigate the effect of particle size on other properties like the bulk modulus and the ratio of the transmitted and applied stress. The bulk modulus describes the compressibility of the material and relates the change in volume of the material, ΔV (m^3), as a function of change in pressure, ΔP (MPa). The bulk modulus is given by:

$$B_{ep} = \frac{\Delta P}{\frac{\Delta V}{V_0}} \quad (9)$$

where B_{ep} represents the bulk modulus taking into account elastic and plastic behaviour (MPa) and all the other variables have been previously defined. This pa-

parameter evolves during loading and is an indicator of deformation in the granular sample.

Lastly, we look at frictional effects by monitoring the transmitted stress ratio, T . To do this, we calculate the ratio of transmitted stress, σ_t (MPa), over the applied stress, σ_a (MPa). The applied stress is outputted from the top axial load washer while the transmitted stress is recorded by the bottom axial load washer. The difference in applied and transmitted stresses provides insight on how much energy is lost to friction in the crucible apparatus. This ratio is given by:

$$T = \frac{\sigma_t}{\sigma_a} \quad (10)$$

To account for the uncertainty in the experiment, we conducted a systematic propagation of error, taking into account the uncertainty of the sensors and measured geometries. This will help in understand the accuracy of our results. Based on the guide outlined by [39], Table 5 summarizes the relative uncertainty of critical material parameters that were calculated. The rules for calculating uncertainty have been derived and computed extensively in literature and will not be explicitly shown. Refer to [39] for full derivations.

2. Experimental Outcome

All compression tests were plotted to underline the variability at a given average particle size. After characterizing the material using standard sieves, a notable variability exists. This should be considered when manufacturing ceramic components through powder compaction.

2.1. Porosity Curve

First, the hydro-static response as a function of porosity and particle size in alumina was investigated, Figure 4. Figure 4(a) depicts the smallest particle sizes ($170 \pm 63 \mu\text{m}$) and Figure 4(d) depicts the biggest particle sizes ($450 \pm 83 \mu\text{m}$). As the particle size is decreased, the curve shifts to the right, with values of porosity for an average hydro-static pressure of 375 MPa reported of $27 \pm 4 \%$ for $170 \pm 63 \mu\text{m}$, $22 \pm 2 \%$ for $230 \pm 55 \mu\text{m}$, $20 \pm 3 \%$ for $330 \pm 67 \mu\text{m}$, and $12 \pm 1 \%$ for $450 \pm 83 \mu\text{m}$. We note the variabilities for a given particle size at this hydro-static pressure, and that not all tests begin at the same initial porosities ϕ_i .

Next, shown in Figure 5 are the hydro-static pressure-porosity curves as a function of particle size for boron carbide. In Figure 5(a), the smaller particles ($170 \pm 40 \mu\text{m}$) are shown, and the larger particle ($470 \pm 90 \mu\text{m}$) are shown in Figure 5(d). From Figure 5, we observe that the curves shift to the right for increasing particle size. For the same average hydro-static pressure of 375 MPa, we find that the resulting porosity is $18 \pm 2 \%$ for particle size $170 \pm 40 \mu\text{m}$, $20 \pm 1 \%$ for $190 \pm 34 \mu\text{m}$, and $25 \pm 2 \%$ for $320 \pm 59 \mu\text{m}$. Since there is only one test for $470 \pm 90 \mu\text{m}$, not much significance is put on it. However, this data is still plotted with the other particle size data-set for completeness. It is important to note that lower porosities were achieved for the Al_2O_3 powder compared to the B_4C even though the applied load was the same.

2.2. Bulk Modulus

Next, we discuss the compaction effects of the materials described by the bulk modulus in Figure 6 and Figure 7 for alumina and boron carbide respectively. Referring to Figure 6, the behaviour of Al_2O_3 particles do not follow a distinct trend in that the bulk modulus is not greater or lesser depending on the particle size. Gen-

erally, the average bulk modulus at the chosen hydro-static pressure of 400 MPa is 988 MPa for $170 \pm 63 \mu\text{m}$, 873 MPa for $230 \pm 55 \mu\text{m}$, 959 MPa for $330 \pm 67 \mu\text{m}$. For the largest size ($450 \pm 83 \mu\text{m}$), the average maximum hydro-static pressure reached was 347 MPa and the corresponding average bulk modulus was 869 MPa. Conversely, clear trends exist when looking at the bulking effects as a function of hydro-static pressure for the B_4C in Figure 7. Namely, the bulk appears to increase with increasing particle size, meaning the material behaviour becomes stiffer for increasing particle size. Furthermore, we can note that higher overall bulk modulus was achieved for the B_4C powder in comparison to the Al_2O_3 powder. At a hydro-static pressure of 400 MPa a bulk modulus of 1031 MPa for $170 \pm 40 \mu\text{m}$, 1164 MPa for $190 \pm 34 \mu\text{m}$, and 1270 MPa for $320 \pm 59 \mu\text{m}$. As mentioned before, there is only one test for $470 \pm 90 \mu\text{m}$ where the bulk modulus of 1387 MPa was reached with a hydro-static pressure of 295 MPa, and so the data-set is only plotted for completeness.

2.3. Transmission Ratio

The transmission ratio relates the force transferred from the compression machine through the material. In Figure 8, we plot the transmission ratio for the Al_2O_3 powder as a function of applied stress. With the applied load below 600 MPa, the trend observed is when increasing the particle size, the transmission ratio increases. This is believed to be a consequence of the larger particles having a smaller contact area that result in less friction, and consequently, for more stress being transmitted. For higher applied stress (1600 MPa) the average transmission ratio for each particle size converges to: 0.35 for $170 \pm 63 \mu\text{m}$, 0.37 for $230 \pm 55 \mu\text{m}$, 0.38 for $330 \pm 67 \mu\text{m}$, and 0.50 for $450 \pm 83 \mu\text{m}$. Unlike the Al_2O_3 , there appears to be no clear trend in the B_4C transmission ratio behaviour, depicted in Figure 9. Taken at 1600 MPa, the average ratio for $170 \pm 40 \mu\text{m}$ is 0.33, for $190 \pm 34 \mu\text{m}$ is 0.32, for $320 \pm 59 \mu\text{m}$ is

1
2
3
4
5 0.31, and for $470 \pm 90 \mu\text{m}$ particle size, there was only one test and so we only plot
6 for completeness.
7

8 9 10 *2.4. Failure*

11 Now that mechanical properties have been explored, we seek to link failure pro-
12 cesses to our material response, and this is done by investigating SEM images in
13 Figure 1 and Figure 2. Recalling that the fragment size, shape, and internal fea-
14 ture morphologies were already presented for Figure 1(a) and discussed in the Sec-
15 tion 1.2.1, we investigate failure and fragmentation features in alumina in Figure 1(b).
16 The particles no longer appear to have elongated structures and have been reduced
17 to shapes having a aspect ratio closer to 1. Shown in Figure 1(c) is a collection
18 of alumina fragments post-experiment for an initial particle size of $450 \pm 83 \mu\text{m}$.
19 From the image, we see that most of the fragments now appear with fewer smaller
20 fragments. In the image, we see that there are few large particles between $150 \mu\text{m}$
21 and $366 \mu\text{m}$ in size, with many more smaller fragments that are between $40 \mu\text{m}$ and
22 $88 \mu\text{m}$ in size. Similar observations were made by [19], where a great amount of fine-
23 grained fragments were recovered post compression. Lastly, shown in Figure 1(d)
24 is an higher magnification SEM image of an alumina fragment surface for the test
25 with initial particle sizes $450 \pm 83 \mu\text{m}$. The image depicts two sets of near parallel
26 fractures emerging from a central crack that spans from right to left in the image.
27 These fractures are interpreted to be a consequence of bending resulting from the
28 elongated initial particle shape for this material
29
30
31
32
33
34
35
36
37
38
39
40
41
42
43

44 Next, we investigate similar failure and fragmentation features in boron carbide
45 in Figure 2(c) and Figure 2(d). Recall, the SEM image in Figure 2(a) and Fig-
46 ure 2(b) depicts typical fragments for a particle size of $170 \pm 40 \mu\text{m}$ and 320 ± 59
47 μm , respectively, demonstrating some block like fragments for sizes of $170 \pm 40 \mu\text{m}$
48
49
50
51
52

1
2
3
4
5 but mostly near-spherical particles with aspect ratios close to 1 for sizes of 320 ± 59
6 μm and $470 \pm 90 \mu\text{m}$. Shown in Figure 2(c) is a collection of fragments taken after
7 an experiment for the $320 \pm 59 \mu\text{m}$ particle size. In the image, we see that there
8 are very few larger block like fragments that are between $175 \mu\text{m}$ and $336 \mu\text{m}$ in size.
9 These larger fragments have some fractures in them and many smaller comminuted
10 fragments in their surface. There are also many smaller fragments between $30 \mu\text{m}$
11 and $82 \mu\text{m}$ in size that are plate-like and angular. Lastly, we depict an SEM image
12 of a fragment surface for a particle that was $320 \pm 59 \mu\text{m}$ in size in Figure 2(d). The
13 fragment surface further highlights some shallow surface fracturing and the presence
14 of many smaller comminuted fragments that are $0.1 \mu\text{m}$ to $2 \mu\text{m}$ in size.
15
16
17
18
19
20
21
22
23

24 2.5. Distributions

25
26 To track the evolution particle size distributions as a consequence of compaction,
27 measurements were taken of the materials before and after compression. To do this,
28 we show the cumulative distribution of the particle sizes taken as the maximum span-
29 ning length provided by the Morphologi G3 microscope and the Microtrac PartAn
30 3-D microscope. The cumulative distribution is defined as:
31
32
33
34
35

$$36 G(x) = \int_0^x g(\bar{x})d\bar{x} \quad (11)$$

37
38 where $g(\bar{x})$ is the probability distribution of the particle sizes. The particle size
39 data set in each direction is a discrete set of n particles with sizes of $l_i (i = 1 \dots n)$.
40 Ordering this data for increasing particle size, and assigning a probability of $1/n$
41 to each particle, the normalized empirical cumulative distribution function can be
42
43
44
45
46
47
48
49
50
51
52

1
2
3
4
5 computed as the sum of these probabilities:
6
7

$$G_e(l) = \frac{1}{n} \sum_{i=1}^n I(l_i \leq l) \quad (12)$$

8
9
10
11

12 where the indicator function I has a value of 1 if $l_i \leq l$ and 0 otherwise. Shown in
13 Figure 10 are the cumulative distributions of particle sizes before and after for the
14 alumina experiments. To generate the figure, characterization pre-experiment was
15 done on the bulk sample, while post-test characterization was done for each of the
16 three repeated experiments (test 01, test 02, test 03). The average of the medians
17 after compression (50th percentiles) are: $7.0 \pm 0.2 \mu\text{m}$ for the $133 \pm 38 \mu\text{m}$ particles,
18 $6.0 \pm 0.1 \mu\text{m}$ for the $201 \pm 42 \mu\text{m}$ particles, $5.0 \pm 0.1 \mu\text{m}$ for the $290 \pm 52 \mu\text{m}$ parti-
19 cles, and $6.0 \pm 0.1 \mu\text{m}$ for the $414 \pm 57 \mu\text{m}$ particles. In Figures 10 and 11, the lower
20 limit of $\sim 2 \mu\text{m}$ is related to our resolution of the particle characterization equipment
21 (corresponding to 8 pixels of an individual particle). While the upper limit appears
22 to be $\sim 50 \mu\text{m}$, there are actually particles upwards of $120 \mu\text{m}$ in size for all post-test
23 samples. Similarly, shown in Figure 11 are the cumulative distributions of particle
24 sizes before and after for the boron carbide experiments. As before, characterization
25 pre-experiment was done on the bulk sample, while post-test characterization was
26 done for each of the three repeated experiments (test 01, test 02, test 03). The
27 average of the medians after compression (50th percentiles) are: $5.0 \pm 0.1 \mu\text{m}$ for the
28 $152 \pm 26 \mu\text{m}$ particles, $5.0 \pm 0.4 \mu\text{m}$ for the $171 \pm 23 \mu\text{m}$ particles, $5.0 \pm 0.3 \mu\text{m}$ for
29 the $303 \pm 46 \mu\text{m}$ particles, and $5.0 \pm 0 \mu\text{m}$ standard deviation for the $461 \pm 44 \mu\text{m}$
30 particles. Generally, trends in the change in sizes or final sizes are challenging to
31 unravel given the different initial starting sizes and porosities, and final hydro-static
32 pressures experienced by the compacted materials.
33
34
35
36
37
38
39
40
41
42
43
44
45
46
47
48
49
50
51
52

3. Discussion

In this paper we explored the mechanical response of alumina and boron carbide powder, in hopes of better understanding the effects of particle size and shape on the uniaxial compaction response under quasi-static strain rates. In the literature, there exists limited studies on the behaviour of granular ceramics [20, 22, 34, 40–42], with many authors noting as much [43, 44]. Few studies have accounted for particle size effects [45, 46]. To address the gap in understanding granular ceramic behaviour, this study focused on the mechanical response (e.g., hydro-static pressure, bulk modulus, transmission ratio) and failure of granular alumina and boron carbide materials of varying particle sizes. The particle size ranges for alumina powder were 107 μm to 533 μm , and for boron carbide were 130 μm to 560 μm . The particle size ranges were chosen based on resulting fragmentation sizes derived during impact into boron carbide by [47], as well to compare with other studies in the literature on granular compaction of comparable sizes (e.g., [20, 48]). Also note that the alumina particles were mostly elongated in shape while the boron carbide fragments has aspect ratios closer to 1. The selection of an elongated shape for particles is also motivated by the impact fragmentation work by [47] where shard-like fragments were observed as a consequence of ballistic testing, while the choice of uniform shapes is to conform with geometries commonly selected in the literature for studies on granular compaction [21, 49]. To study the uniaxial confined response of the materials, an apparatus for confined quasi-static compression was designed and adapted from literature [50–52]. Other studies in the literature have used different experimental approaches, including the thick-walled cylinder set-ups for confined uniaxial compaction under quasi-static and dynamic loading [19], plate impact testing [9], and thick-walled implosion compaction experiments [53]. In thick-walled cylinder implosion experiments performed

1
2
3
4
5 on granular alumina by [53] and silicon carbide by [45], both noted the importance
6 of shear localization and comminution in the responses of granular ceramics. We
7 also note the importance of comminution in our quasi-static confined compaction
8 experiments, as evidenced by Figure 1 and Figure 2.
9
10

11
12 To better understand the effect of particle size on the mechanical response, in-
13 vestigations were made on the bulk modulus and transmission ratio as a function of
14 pressure. For bulk modulus, the Al_2O_3 did not exhibit any clear trends in behaviour
15 as a function of particle size, while the boron carbide demonstrated a greater sensitiv-
16 ity of the bulk modulus on hydro-static pressure (steeper slope) and an overall greater
17 bulk modulus as a function of increasing particle size (1031 ± 72 MPa for 170 ± 40
18 μm , 1164 ± 50 MPa for 190 ± 34 μm , and 1270 ± 136 MPa for 320 ± 59 μm). These
19 values align with those reported in literature by [54]. For the transmission ratio,
20 which probed the effects of friction, clear trends were observed in the alumina ma-
21 terial (0.35 ± 0.01 for 170 ± 63 μm , 0.370 ± 0.006 for 230 ± 55 μm , 0.38 ± 0.01 for
22 330 ± 67 μm , and 0.50 ± 0.06 for 450 ± 83 μm) where similarities have been observed
23 before [55, 56]. Specifically, these values align with those reported by [56] of ~ 0.4
24 at 100 MPa. Boron carbide, on the other hand, did not exhibit clear trends which
25 has not been noted previously. Generally, the high variability across all mechanical
26 property measurements is likely a consequence of the variable spatial distribution of
27 particle size and shape distributions among samples as a result of sample preparation
28 and setup.
29
30
31
32
33
34
35
36
37
38
39
40
41
42

43 In addition to probing the effects of particle size on bulk modulus and transmis-
44 sion ratio, we also explored the effects of particle size on the hydro-static response as
45 a function of porosity. This relation is important when developing yield surfaces for
46 brittle failure [46, 57, 58]. Two distinct trends were observed from our experiments.
47 In the alumina samples with elongated particle shape, increasing the particle size
48
49
50
51
52

1
2
3
4
5 resulted in the curve shifted to the left. At 375 MPa, the porosity was observed to
6 decrease for increasing particle size (27 ± 4 % porosity at 170 ± 63 μm , to 12 ± 1 %
7 porosity at particle size 450 ± 83 μm). Conversely for boron carbide, as the parti-
8 cle size increased from 170 ± 40 μm to 470 ± 90 μm , less porosity was crushed out
9 (18 ± 2 % for particle size 170 ± 40 μm , to 25 ± 2 % for particle size 320 ± 59 μm).
10 Additionally, the spread of the hydro-static curves for repeated experiments for B_4C
11 was smaller in comparison to Al_2O_3 . Comparing the results from our study, [49]
12 conducted similar confined compaction tests of alumina powder for the purpose of
13 investigating the effects of compaction stress on granular rearrangement. They noted
14 that when increasing the sample diameter, the required compaction stress decreases
15 as a result of a decrease in the die wall friction. Notably, for a compaction stress
16 of ~ 100 MPa and alumina powder size of 75 μm to 150 μm with 2% binder, [49] re-
17 ported a porosity of 43%. In our experiments involving 170 μm powders, we were
18 able to achieve 41% porosity at the same hydro-static pressure. Taken together,
19 the results demonstrate the sensitivity of particle size on mechanical responses, and
20 this highlights the importance incorporating these considerations into failure models.
21 This is discussed next.
22
23
24
25
26
27
28
29
30
31
32
33
34
35

36 In addition comparing our data with other experiments in the literature, there
37 are numerous modelling approaches in the literature that attempt to describe granu-
38 lar compaction and comminution [44, 57, 59], with some models requiring adjustable
39 parameters that have no fundamental physical basis [60]. Classical failure models
40 often do not account for grain size but rather only account for strength to void ra-
41 tios [61]. Recently, a study by [43] noted the importance of incorporating relative
42 density, porosity, particle size distribution, and particle breakage into constitutive
43 modelling of brittle granular materials. The micro-mechanical model of [43] is refer-
44 ed to as a breakage model, and it initially was developed for soil mechanics [62–64].
45
46
47
48
49
50
51
52

The breakage term, described by (13), represents as an internal state variable in a computational modelling framework that accounts for how the particle sizes evolve and become smaller during loading. The breakage model is given by [43]:

$$B_r = \frac{\int_{d_m}^{d_M} (F(d) - F_0(d))d^{-1}dd}{\int_{d_m}^{d_M} (F_u(d) - F_0(d))d^{-1}dd} \quad (13)$$

The relative breakage term is integrated between the grain size, $d_{m,M}$, over the initial distribution $F_0(d)$, current distribution $F(d)$, and ultimate distribution $F_u(d)$. $F_0(d)$ can be measured before each experiment, although in this study we did random sampling of the suite of experiments at given size to measure those size distributions. $F(d)$ represents the size distribution at an intermediate state (e.g., Figure 10 & Figure 11). From the current experiments, $F_u(d)$ is unknown, however it may take a similar functional form to those in Figure 10 and Figure 11 for $F(d)$. Note that many fits (e.g., Weibull, log-normal, exponential) were attempted for the data in Figures 10 and 11, and none provided adequate description of the data. In a study by [65], tests were performed to various strains and particle sizes measured, $F_u(d)$ was assumed to take the functional form of $\frac{d}{d_M}^{3-\alpha}$ where α is a constant, and the breakage model form was derived. Notable in the results presented in the paper by [65] and others in the literature [43] is that it is commonly assumed that the lower and upper bound of the size distributions in $F_0(d)$, $F(d)$, and $F_u(d)$ remain the same during compaction. Our results on alumina and boron carbide show that the lower and upper bounds likely changes during compaction, and so that raises the question of how these distributions evolve. Unravelling the path of breakage warrants future work given the complexity of the competition between scale-dependent compaction, flow, fracture, comminution, and surface abrasion.

Lastly, the [43] study highlighted the complex nature of granular ceramics expe-

1
2
3
4
5
6
7
8
9
10
11
12
13
14
15
16
17
18
19
20
21
22
23
24
25
26
27
28
29
30
31
32
33
34
35
36
37
38
39
40
41
42
43
44
45
46
47
48
49
50
51
52
53
54
55
56
57
58
59
60

riencing multi-axial loading conditions during projectile impact and introduced the breakage model as a potential solution. However, as evident by the [43] study and others ([23, 44]), limited experimental data for granular advanced ceramics exists for parametrizing the breakage model and often times sand is used as a substitute. Sand is likely not a good analogue for accurate parameterization when modelling advanced ceramics. The work presented in this study builds from the validation attempts conducted by [43]. Beyond this, the data for hydro-static pressure response as a function of porosity provided in this study can verify the particle gradation parameter; this will be valuable in the literature.

4. Conclusion

Uniaxial quasi-static compression experiments were conducted using a uniaxial compaction technique to determine the triaxial behaviour of granular Al_2O_3 and B_4C as a function of particle size and shape. The results showed an influence of particle size in the compaction curves where porosity is related as a function of hydro-static pressure, the bulk modulus is related to hydro-static pressure, and the transmission ratio is related to the applied stress. The elongated Al_2O_3 powder showed large variations among each sample tested for the hydro-static response, while the B_4C powder, with an aspect ratio close to 1, was less variable. In the bulk modulus response of both materials, the alumina showed no clear trend as a function of particle size. Observing the B_4C response, we see that as the particle size increases the change in the bulk modulus increases in addition to a vertical shift of the material trends. When observing the transmission ratio results for the Al_2O_3 powder, below 600 MPa the larger particles allow for more stress to be transmitted. At higher applied stresses the trend observed is with increasing particle size the transmission ratio increases. In comparison, no clear particle size dependent trends are observed in B_4C . These

1
2
3
4
5 trends are thought to be influenced by the failure exhibiting in the material during
6 compaction. SEM images of both materials provide evidence of micro cracking and
7 fragmentation during the quasi-static confined compression. Further research must
8 be conducted to better understand the particle size dependencies on mechanical
9 properties of granular Al_2O_3 and B_4C , so that a better understanding is established
10 on the failure regimes seen during triaxial loading conditions.
11
12
13
14
15
16

17 **5. Acknowledgments**

18
19
20 This research was sponsored by the Army Research Laboratory and was accom-
21 plished under Cooperative Agreement Number W911NF-12-2-0022. The opinions
22 and conclusions contained in this document are those of the authors and should not
23 be interpreted as representing the official policies, either expressed or implied, of the
24 Army Research Laboratory or the United States Government. The United States
25 Government is authorized to reproduce and distribute reprints for Government pur-
26 poses notwithstanding any copyright notation herein. Furthermore, this article was
27 also supported by the Ministry of Education, Science, Research and Sport of the Slo-
28 vak Republic within the Research and Development Operational Programme for the
29 project “University Science Park of STU Bratislava”, ITMS 26240220084, co-funded
30 by the European Regional Development Fund. Lastly, The author(s) would also like
31 to express their support to Dr. Roman Fekete and the Slovak University of Tech-
32 nology in Bratislava for their help in conducting the compression experiments and
33 providing insights on granular compression.
34
35
36
37
38
39
40
41
42
43
44
45
46
47
48
49
50
51
52
53
54
55
56
57
58
59
60

References

- [1] Ryan EV. Asteroid Fragmentation and Evolution of Asteroids. *Annual Review of Earth and Planetary Sciences*. 2000 May;28(1):367–389.
- [2] Singh PK, Roy MP, Paswan RK, Sarim M, Kumar S, Ranjan Jha R. Rock Fragmentation Control in Opencast Blasting. *Journal of Rock Mechanics and Geotechnical Engineering*. 2016 Apr;8(2):225–237.
- [3] Figueiredo ABHdS, Lima Júnior EP, Gomes AV, de Melo GBM, Monteiro SN, de Biasi RS. Response to Ballistic Impact of Alumina-UHMWPE Composites. *Materials Research*. 2018 Aug;21(5).
- [4] Medvedovski E. Ballistic Performance of Armour Ceramics: Influence of Design and Structure. Part 2. *Ceramics International*. 2010;36(7):2117–2127.
- [5] Asenov S, Lakov L, Toncheva K. Promising Ceramic Materials for Ballistic Protection. 2013;p. 6.
- [6] Walley SM. Historical Review of High Strain Rate and Shock Properties of Ceramics Relevant to Their Application in Armour. *Advances in Applied Ceramics*. 2010 Nov;109(8):446–466.
- [7] Lane R, Craig B, Babcock W. Materials for Blast and Penetration Resistance. 2001;6(4):7.
- [8] Behner T, Heine A, Wickert M. Dwell and Penetration of Tungsten Heavy Alloy Long-Rod Penetrators Impacting Unconfined Finite-Thickness Silicon Carbide Ceramic Targets. *International Journal of Impact Engineering*. 2016 Sep;95:54–60.

- 1
2
3
4
5 [9] Behner T, Heine A, Wickert M. Dwell and Penetration of Tungsten Heavy Alloy
6 Long-Rod Penetrators Impacting Unconfined Finite-Thickness Silicon Carbide
7 Ceramic Targets. *International Journal of Impact Engineering*. 2016 Sep;95:54-
8 60.
9
10
11
12
13 [10] Krell A, Strassburger E. Order of Influences on the Ballistic Resistance of
14 Armor Ceramics and Single Crystals. *Materials Science and Engineering: A*.
15 2014 Mar;597:422-430.
16
17
18
19 [11] Hogan JD, Farbaniec L, Mallick D, Domnich V, Kuwelkar K, Sano T, et al. Frag-
20 mentation of an Advanced Ceramic under Ballistic Impact: Mechanisms and
21 Microstructure. *International Journal of Impact Engineering*. 2017 Apr;102:47-
22 54.
23
24
25
26
27 [12] Shockey DA, Marchand AH, Skaggs SR, Cort GE, Burkett MW, Parker R.
28 Failure Phenomenology of Confined Ceramic Targets and Impacting Rods. *In-*
29 *ternational Journal of Impact Engineering*. 1990;9(3):263-275.
30
31
32
33 [13] Grady DE. Fragmentation of Solids under Impulsive Stress Loading. *Journal of*
34 *Geophysical Research: Solid Earth*. 1981 Feb;86(B2):1047-1054.
35
36
37
38 [14] Farbaniec L, Hogan JD, Xie KY, Shaeffer M, Hemker KJ, Ramesh KT. Damage
39 Evolution of Hot-Pressed Boron Carbide under Confined Dynamic Compression.
40 *International Journal of Impact Engineering*. 2017 Jan;99:75-84.
41
42
43
44 [15] Hogan JD, Robinson AK, Tilson J, Krimsky E, Ramesh KT. On the Behavior
45 of Fragmented Brittle Materials. 2015 Jun;.
46
47
48
49 [16] Mott NF, Linfoot EH, Grady D. In: *A Theory of Fragmentation*; 2006. p.
50 207-225.
51
52

- 1
2
3
4
5 [17] Grady DE, Kipp ME. Mechanisms of Dynamic Fragmentation: Factors Gov-
6 erning Fragment Size. 1985;p. 4.
7
8
9
10 [18] Hogan J, Farbaniec L, Shaeffer M, Ramesh KT. The Effects of Microstructure
11 and Confinement on the Compressive Fragmentation of an Advanced Ceramic.
12 Journal of the American Ceramic Society. 2014 11;98.
13
14
15
16 [19] Meyer LW, Faber I. Investigations on Granular Ceramics and Ceramic Powder.
17 Le Journal de Physique IV. 1997;7(C3):C3-565.
18
19
20 [20] Vogler TJ, Lee MY, Grady DE. Static and Dynamic Compaction of Ceramic
21 Powders. International Journal of Solids and Structures. 2007 Jan;44(2):636-
22 658.
23
24
25
26 [21] Choudhary A, Ramavath P, Biswas P, Ravi N, Johnson R. Experimental Investi-
27 gation on Flowability and Compaction Behavior of Spray Granulated Submicron
28 Alumina Granules. ISRN Ceramics. 2013;2013:1-6.
29
30
31
32 [22] Huang JY, Hu SS, Xu SL, Luo SN. Fractal Crushing of Granular Materials
33 under Confined Compression at Different Strain Rates. International Journal of
34 Impact Engineering. 2017 Aug;106:259-265.
35
36
37
38 [23] Curran DR, Seaman L, Cooper T, Shockey DA. Micromechanical Model for
39 Comminution and Granular Flow of Brittle Material under High Strain Rate
40 Application to Penetration of Ceramic Targets. International Journal of Impact
41 Engineering. 1993 Jan;13(1):53-83.
42
43
44
45 [24] Ashby MF, Hallam (Née Cooksley) SD. The Failure of Brittle Solids Contain-
46 ing Small Cracks under Compressive Stress States. Acta Metallurgica. 1986
47 Mar;34(3):497-510.
48
49
50
51
52

- 1
2
3
4
5 [25] Fredrich JT, Evans B, Wong TF. Effect of Grain Size on Brittle and Semibrittle
6 Strength: Implications for Micromechanical Modelling of Failure in Compres-
7 sion. *Journal of Geophysical Research*. 1990;95(B7):10907.
8
9
10
11 [26] Awasthi A, Wang Z, Broadhurst N, Geubelle P. Impact Response of Granular
12 Layers. *Granular Matter*. 2015 Feb;17(1):21–31.
13
14
15
16 [27] Homel MA, Guilkey JE, Brannon RM. Continuum Effective-Stress Approach for
17 High-Rate Plastic Deformation of Fluid-Saturated Geomaterials with Applica-
18 tion to Shaped-Charge Jet Penetration. *Acta Mechanica*. 2016 Feb;227(2):279–
19 310.
20
21
22
23
24 [28] Sørensen JD, Burcharth HF. Reliability Analysis of Geotechnical Failure Modes
25 for Vertical Wall Breakwaters. *Computers and Geotechnics*. 2000 Apr;26(3-
26 4):225–245.
27
28
29
30 [29] Fossum AF, Brannon RM. On a Viscoplastic Model for Rocks with Mechanism-
31 Dependent Characteristic Times. *Acta Geotechnica*. 2006 Sep;1(2):89–106.
32
33
34
35 [30] Holmquist TJ, Johnson GR. The Failed Strength of Ceramics Subjected to
36 High-Velocity Impact. *Journal of Applied Physics*. 2008 Jul;104(1):013533.
37
38
39 [31] Cacace S, Demir AG, Semeraro Q. Densification Mechanism for Different
40 Types of Stainless Steel Powders in Selective Laser Melting. *Procedia CIRP*.
41 2017;62:475–480.
42
43
44
45 [32] Hogan J, Robinson A, Tilson J, Krinsky E, Ramesh KT. On the Behavior of
46 Fragmented Brittle Materials; 2015. .
47
48
49
50
51
52

- 1
2
3
4
5 [33] Wang H, Ramesh KT. Dynamic Strength and Fragmentation of Hot-Pressed Silicon Carbide under Uniaxial Compression. *Acta Materialia*. 2004 Jan;52(2):355–
6
7
8
9
10
11
12 [34] Dannemann K. Ceramic Phenomenological Experiments- Compressive Strength
13
14
15
16 [35] Hackley VA, Ferraris CF. The Use of Nomenclature in Dispersion Science and
17
18
19
20
21 [36] Maynard E. Five Fundamentals for Effective Blend Sampling;p. 3.
22
23 [37] Engeli R, Etter T, Hovel S, Wegener K. Processability of Different IN738LC
24
25
26
27
28
29 [38] Fleck NA, Cocks ACF. IUTAM Symposium on Mechanics of Granular and
30
31
32
33
34
35
36
37
38
39
40
41
42 [40] Anderson CE. Compression Testing and Response of SiC-N Ceramics: Intact,
43
44
45
46
47
48
49
50
51
52
53
54
55
56
57
58
59
60

- 1
2
3
4
5 [41] Nemat S, Sarva S. Micro-Mechanisms of Compression Failure. 2002;p. 17.
6
7
8 [42] Lankford J, Predebon WW, Staehler JM, Subhash G, Pletka BJ, Anderson CE.
9 The Role of Plasticity as a Limiting Factor in the Compressive Failure of High
10 Strength Ceramics. *Mechanics of Materials*. 1998;29(3):205–218.
11
12
13
14 [43] Cil MB, Hurley RC, Graham-Brady L. A Rate-dependent Constitutive Model
15 for Brittle Granular Materials Based on Breakage Mechanics. *Journal of the*
16 *American Ceramic Society*. 2019 Mar;p. jace.16376.
17
18
19
20 [44] Klopp RW, Shockey DA. The Strength Behavior of Granulated Silicon Carbide
21 at High Strain Rates and Confining Pressure. *Journal of Applied Physics*. 1991
22 Dec;70(12):7318–7326.
23
24
25
26 [45] Shih CJ, Nesterenko VF, Meyers MA. High-Strain-Rate Deformation and Com-
27 minution of Silicon Carbide. *Journal of Applied Physics*. 1998 May;83(9):4660–
28 4671.
29
30
31
32 [46] Shih CJ, Meyers MA, Nesterenko VF. High-Strain-Rate Deformation of Gran-
33 ular Silicon Carbide. *Acta Materialia*. 1998 Jul;46(11):4037–4065.
34
35
36
37 [47] Hogan JD, Farbaniec L, Mallick D, Domnich V, Kuwelkar K, Sano T, et al. Frag-
38 mentation of an Advanced Ceramic under Ballistic Impact: Mechanisms and
39 Microstructure. *International Journal of Impact Engineering*. 2017 Apr;102:47–
40 54.
41
42
43
44
45 [48] Suescun Florez E, Kashuk S, Iskander M, Bless S. Predicting the Uniaxial
46 Compressive Response of Granular Media over a Wide Range of Strain Rates
47 Using the Strain Energy Density Concept. *Journal of Dynamic Behavior of*
48 *Materials*. 2015 Sep;1(3):330–346.
49
50
51
52

- 1
2
3
4
5 [49] Carneim RD, Messing GL. Response of Granular Powders to Uniaxial Loading
6 and Unloading. 2001;p. 8.
7
8
9
10 [50] Hong ST, Hovanski Y, Lavender CA, Weil KS. Investigation of Die Stress Pro-
11 files During Powder Compaction Using Instrumented Die. Journal of Materials
12 Engineering and Performance. 2008 Jun;17(3):382–386.
13
14
15
16 [51] Lindskog P, Andersson DC, Larsson PL. An Experimental Device for Material
17 Characterization of Powder Materials. Journal of Testing and Evaluation. 2013
18 May;41(3):20120107.
19
20
21
22 [52] Staf H, Olsson E, Lindskog P, Larsson PL. Determination of the Frictional Be-
23 havior at Compaction of Powder Materials Consisting of Spray-Dried Granules.
24 Journal of Materials Engineering and Performance. 2018 Mar;27(3):1308–1317.
25
26
27
28 [53] Nesterenko VF, Meyers MA, Chen HC. Shear Localization in High-Strain-Rate
29 Deformation of Granular Alumina. Acta materialia. 1996;44(5):2017–2026.
30
31
32
33 [54] Dyachkov SA, Parshikov AN, Zhakhovsky VV. SPH Simulation of Boron Car-
34 bide under Shock Compression with Different Failure Models. Journal of Physics:
35 Conference Series. 2017 Feb;815:012012.
36
37
38
39 [55] Briscoe BJ, Rough SL. The Effects of Wall Friction in Powder Compaction. Col-
40 loids and Surfaces A: Physicochemical and Engineering Aspects. 1998 Jun;137(1-
41 3):103–116.
42
43
44
45 [56] Dimilia RA, Reed JS. Stress Transmission During the Compaction of a Spray-
46 Dried Alumina Powder in a Steel Die. Journal of the American Ceramic Society.
47 1983 Sep;66(9):667–672.
48
49
50
51
52

- 1
2
3
4
5 [57] Chocron S, Anderson CE, Dannemann KA, Nicholls AE, King NL. Intact and
6 Predamaged Boron Carbide Strength under Moderate Confinement Pressures.
7 Journal of the American Ceramic Society. 2012 Jan;95(1):350–357.
8
9
10
11 [58] Stupkiewicz S, Piccolroaz A, Bigoni D. Elastoplastic Coupling to Model Cold
12 Ceramic Powder Compaction. Journal of the European Ceramic Society. 2014
13 Sep;34(11):2839–2848.
14
15
16
17 [59] Curran DR, Seaman L, Cooper T, Shockey DA. Micromechanical Model for
18 Comminution and Granular Flow of Brittle Material under High Strain Rate
19 Application to Penetration of Ceramic Targets. International Journal of Impact
20 Engineering. 1993 Jan;13(1):53–83.
21
22
23
24 [60] Carneim RD. Characterization of Uniaxial Compaction in Spray Dried Ceramic
25 Powders;p. 124.
26
27
28
29 [61] Tengattini A, Das A, Einav I. A Constitutive Modelling Framework Predicting
30 Critical State in Sand Undergoing Crushing and Dilation. Géotechnique. 2016
31 Sep;66(9):695–710.
32
33
34
35 [62] Daouadji A, Hicher PY, Rahma A. An Elastoplastic Model for Granular Ma-
36 terials Taking into Account Grain Breakage. European Journal of Mechanics -
37 A/Solids. 2001 Jan;20(1):113–137.
38
39
40
41 [63] Hu W, Yin Z, Dano C, Hicher PY. A Constitutive Model for Granular Mate-
42 rials Considering Grain Breakage. Science China Technological Sciences. 2011
43 Aug;54(8):2188–2196.
44
45
46
47 [64] Kumar R, Ketterhagen W, Sarkar A, Curtis J, Wassgren C. Breakage Model-
48
49
50
51
52
53
54
55
56
57
58
59
60

1
2
3
4
5 ing of Needle-Shaped Particles Using the Discrete Element Method. Chemical
6
7 Engineering Science: X. 2019 Aug;3:100027.
8

9
10 [65] Einav I. Breakage Mechanics—Part I: Theory. Journal of the Mechanics and
11 Physics of Solids. 2007 Jun;55(6):1274–1297.
12
13
14
15
16
17
18
19
20
21
22
23
24
25
26
27
28
29
30
31
32
33
34
35
36
37
38
39
40
41
42
43
44
45
46
47
48
49
50
51
52

Table 1: Al₂O₃ Powder Characterization: the material span is Δ (unit-less), the tenth percentile D_{10} (μm), the fiftieth percentile D_{50} (μm), ninetieth percentile D_{90} (μm), and the aspect ratio with respect to the width and length, w/l , of the distribution.

$\emptyset[\mu\text{m}]$	$D_{10}[\mu\text{m}]$	$D_{50}[\mu\text{m}]$	$D_{90}[\mu\text{m}]$	Δ	w/l
170 ± 63	97	160	240	0.894	0.472 ± 0.2
230 ± 55	170	220	290	0.545	0.490 ± 0.2
330 ± 67	250	310	390	0.452	0.552 ± 0.2
450 ± 83	370	430	520	0.349	0.579 ± 0.2

Table 2: B₄C Powder Characterization: the material span is Δ (unit-less), the tenth percentile D_{10} (μm), the fiftieth percentile D_{50} (μm), ninetieth percentile D_{90} (μm), and the aspect ratio with respect to the width and length, w/l , of the distribution.

$\emptyset[\mu\text{m}]$	$D_{10}[\mu\text{m}]$	$D_{50}[\mu\text{m}]$	$D_{90}[\mu\text{m}]$	Δ	w/l
170 ± 40	130	170	210	0.471	0.515 ± 0.2
190 ± 34	150	180	210	0.333	0.607 ± 0.1
320 ± 59	280	320	370	0.281	0.687 ± 0.1
470 ± 90	430	470	520	0.191	0.769 ± 0.1

Table 3: Al₂O₃ experiment parameters: mean diameter $\bar{\phi}$ (μm), mass m (g), initial void volume V_i (mm³), initial density ρ_i (kg m⁻³), final density ρ_f (kg m⁻³), initial porosity ϕ_i (%), and final porosity ϕ_f (%).

$\bar{\phi}$ [μm]	m [g]	V_i [mm ³]	ρ_i [kg m ⁻³]	ρ_f [kg m ⁻³]	ϕ_i	ϕ_f
170 \pm 63	0.3265	198	1647	3199	58.7%	19.8%
170 \pm 63	0.3249	183	1779	3237	55.4%	18.8%
170 \pm 63	0.3306	188	1758	3439	55.9%	13.7%
230 \pm 55	0.3174	188	1686	3273	57.7%	17.9%
230 \pm 55	0.3327	195	1705	3362	57.2%	15.7%
230 \pm 55	0.3311	204	1626	3581	59.2%	10.2%
330 \pm 67	0.3651	200	1821	3371	54.3%	15.4%
330 \pm 67	0.3587	198	1807	3253	54.7%	18.4%
330 \pm 67	0.3495	176	1991	3552	50.1%	10.9%
450 \pm 83	0.3202	168	1907	3630	52.2%	9.0%
450 \pm 83	0.3062	161	1900	3634	52.3%	8.9%
450 \pm 83	0.3220	164	1963	3722	50.8%	6.7%

Table 4: B₄C experiment parameters: mean diameter \bar{O} (μm), mass m (g), initial void volume V_i (mm^3), initial density ρ (kg m^{-3}), final density ρ (kg m^{-3}), initial porosity ϕ_i (%), and final porosity ϕ_f (%).

\bar{O} [μm]	m [g]	V_i [mm^3]	ρ_i [kg m^{-3}]	ρ_f [kg m^{-3}]	ϕ_i	ϕ_f
170 ± 40	0.2728	201	1359	2228	46.1%	11.6%
170 ± 40	0.2843	221	1287	2135	48.9%	15.3%
170 ± 40	0.2650	197	1349	2232	46.5%	11.4%
190 ± 34	0.2731	200	1364	2132	45.9%	15.4%
190 ± 34	0.2847	202	1410	2189	44.0%	13.1%
190 ± 34	0.2825	200	1409	2099	44.1%	16.7%
320 ± 59	0.2321	207	1121	1777	55.5%	29.5%
320 ± 59	0.2666	191	1393	2148	44.7%	14.8%
320 ± 59	0.2725	196	1393	2118	44.7%	15.9%
470 ± 90	0.1680	201	836	2358	66.8%	6.4%

Table 5: Systematic uncertainty: propagation of error

Constants	Al ₂ O ₃ 170 \pm 63 μm	Al ₂ O ₃ 450 \pm 83 μm	B ₄ C 170 \pm 40 μm	B ₄ C 320 \pm 59 μm
V_o	0.7%	0.7%	0.6%	0.5%
ϕ	2.5%	3.1%	1.7%	1.4%
P	1.2%	1.0%	1.2%	1.5%
B_{ep}	1.9%	1.9%	1.8%	1.5%
T	1.9%	1.9%	2.0%	2.9%

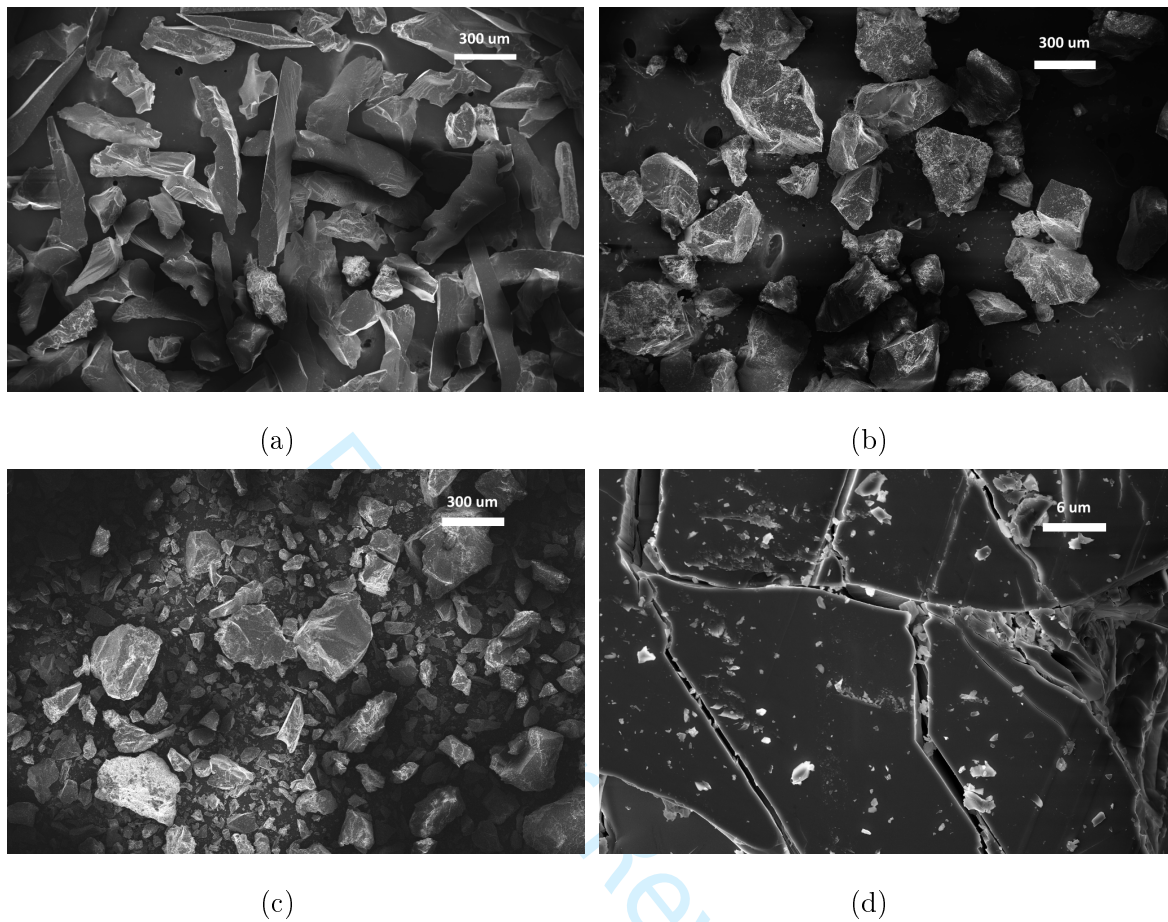


Figure 1: SEM images were taken of the Al₂O₃ powder to observe powder morphology before experiments and failure features post-experiment. (a) depicts the Al₂O₃ powder ($170 \pm 63 \mu\text{m}$) before compression. (b) depicts the Al₂O₃ powder ($170 \pm 63 \mu\text{m}$) after compression. Lastly, position (c) depicts the large Al₂O₃ powder ($450 \pm 83 \mu\text{m}$) after the experiment showing the resulting material size and shapes and (d) depicts surface features of the $450 \pm 83 \mu\text{m}$ Al₂O₃ powder.

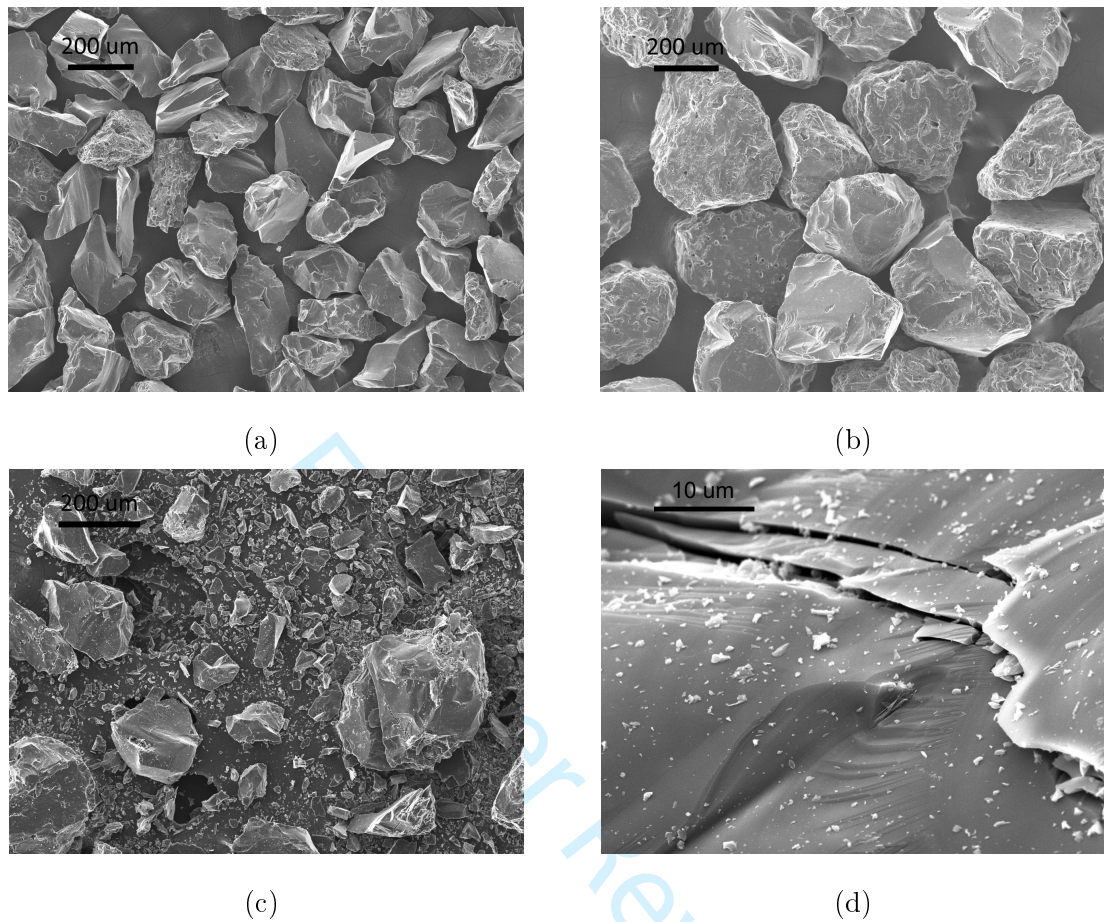


Figure 2: SEM images of B₄C were taken to observe the small and large particles, focusing on powder morphology before and after experiment. Position (a) depicts 170 ± 40 μm B₄C powder before compression. Position (b) depicts the 320 ± 59 μm particle size showing the overall geometry before compression. Position (c) depicts the postmortem 320 ± 59 μm powder visualizing the overall fragment distribution and (d) depicts the surface features post experiment.

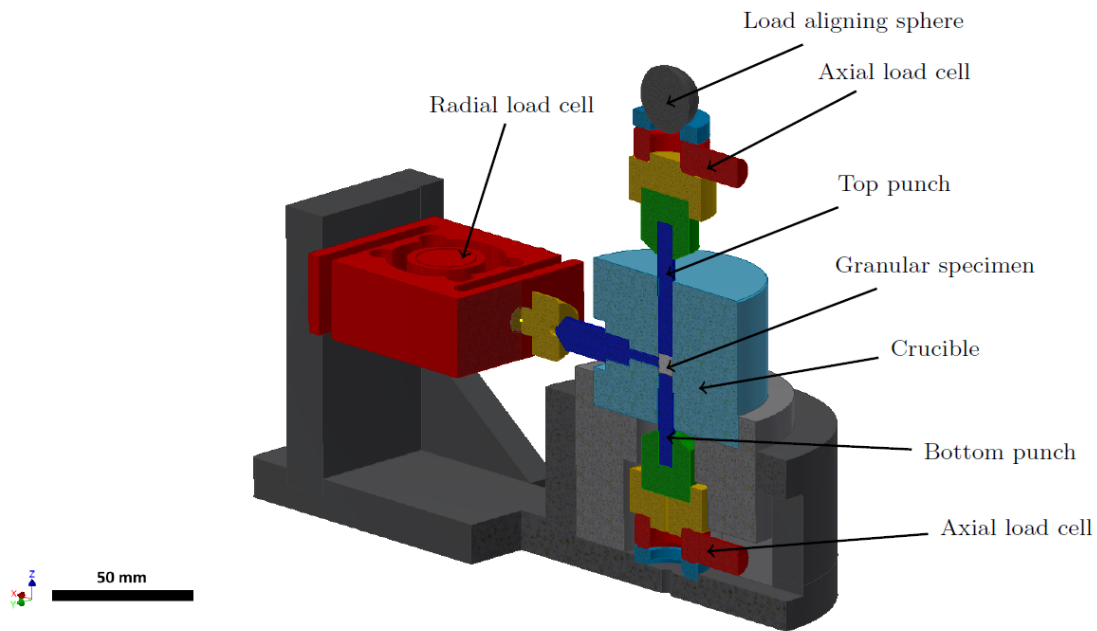


Figure 3: An isometric cross-section view is shown of the compaction apparatus used in compressing Al_2O_3 & B_4C powders to show the different components. The colour in the figure is to distinguish various components that constitute the apparatus.

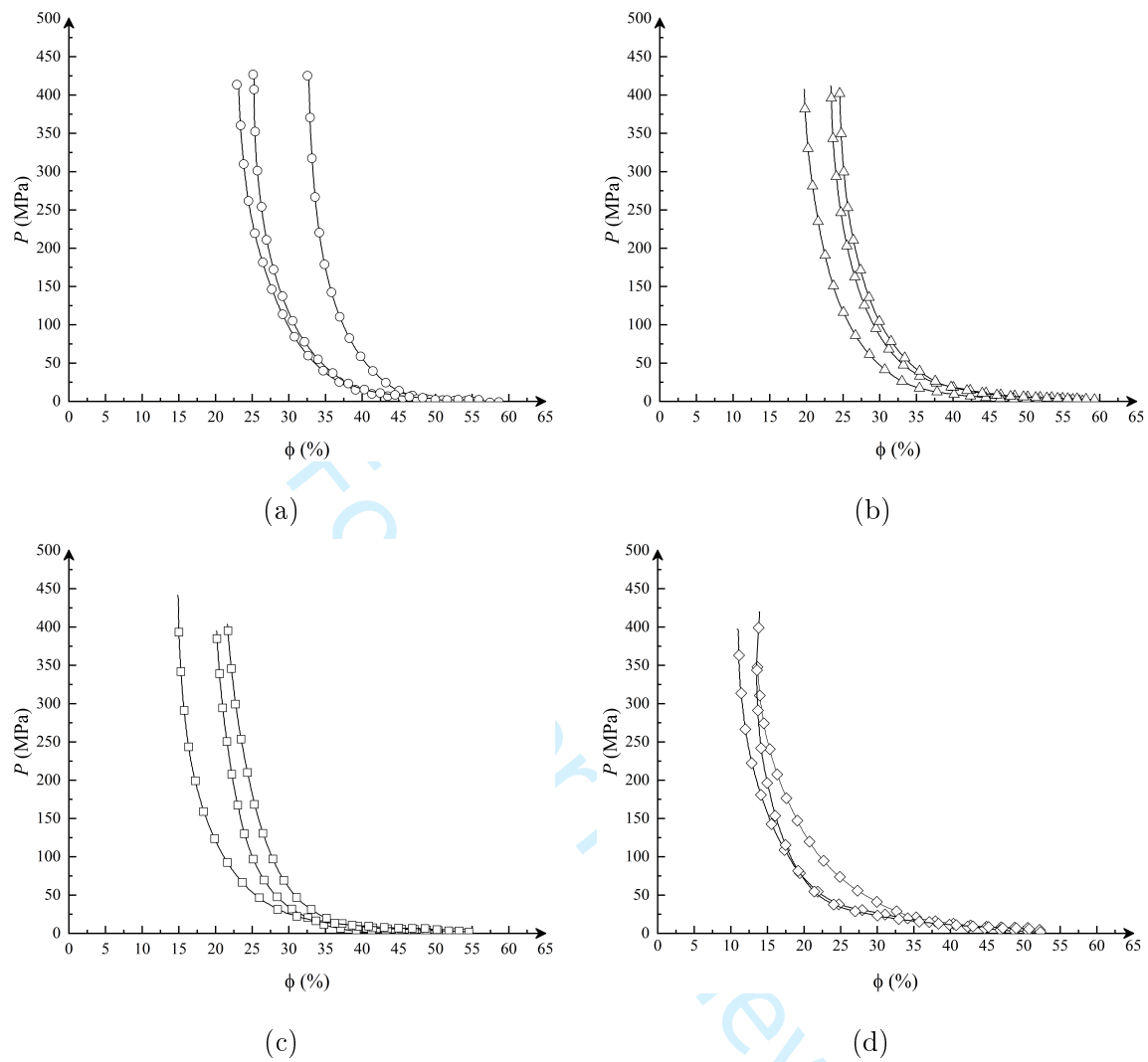


Figure 4: In the figure we see the hydro-static pressure response of granular Al_2O_3 . In (a), the hydro-static pressure response as a function of porosity was captured for the range of particles $170 \pm 63 \mu\text{m}$. In (b), the hydro-static pressure response as a function of porosity was captured for the particle size range $230 \pm 55 \mu\text{m}$. In position (c) the hydro-static pressure response was captured for the particle size range $330 \pm 67 \mu\text{m}$. In position (d), the hydro-static pressure response was captured for particle size range $450 \pm 83 \mu\text{m}$.

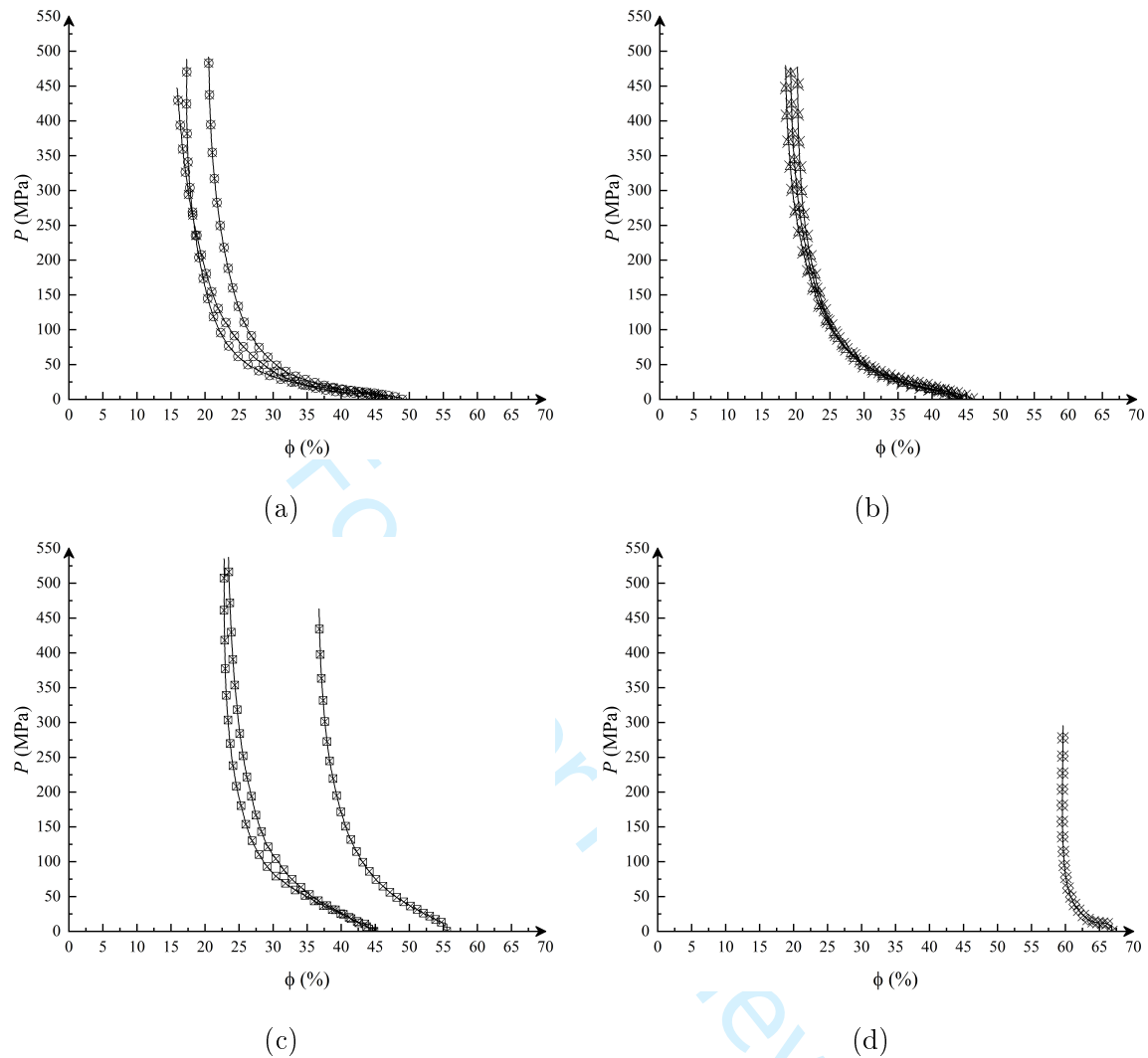


Figure 5: In the figure we see the hydro-static pressure response of granular B_4C . In (a), the hydro-static pressure response as a function of porosity was captured for the range of particles: $170 \pm 40 \mu\text{m}$. In (b), the hydro-static pressure response as a function of porosity was captured for the particle size range: $190 \pm 34 \mu\text{m}$. In position (c) the hydro-static pressure response was captured for the particle size range: $320 \pm 59 \mu\text{m}$. In position (d), the hydro-static pressure response was captured for particle size range: $470 \pm 90 \mu\text{m}$.

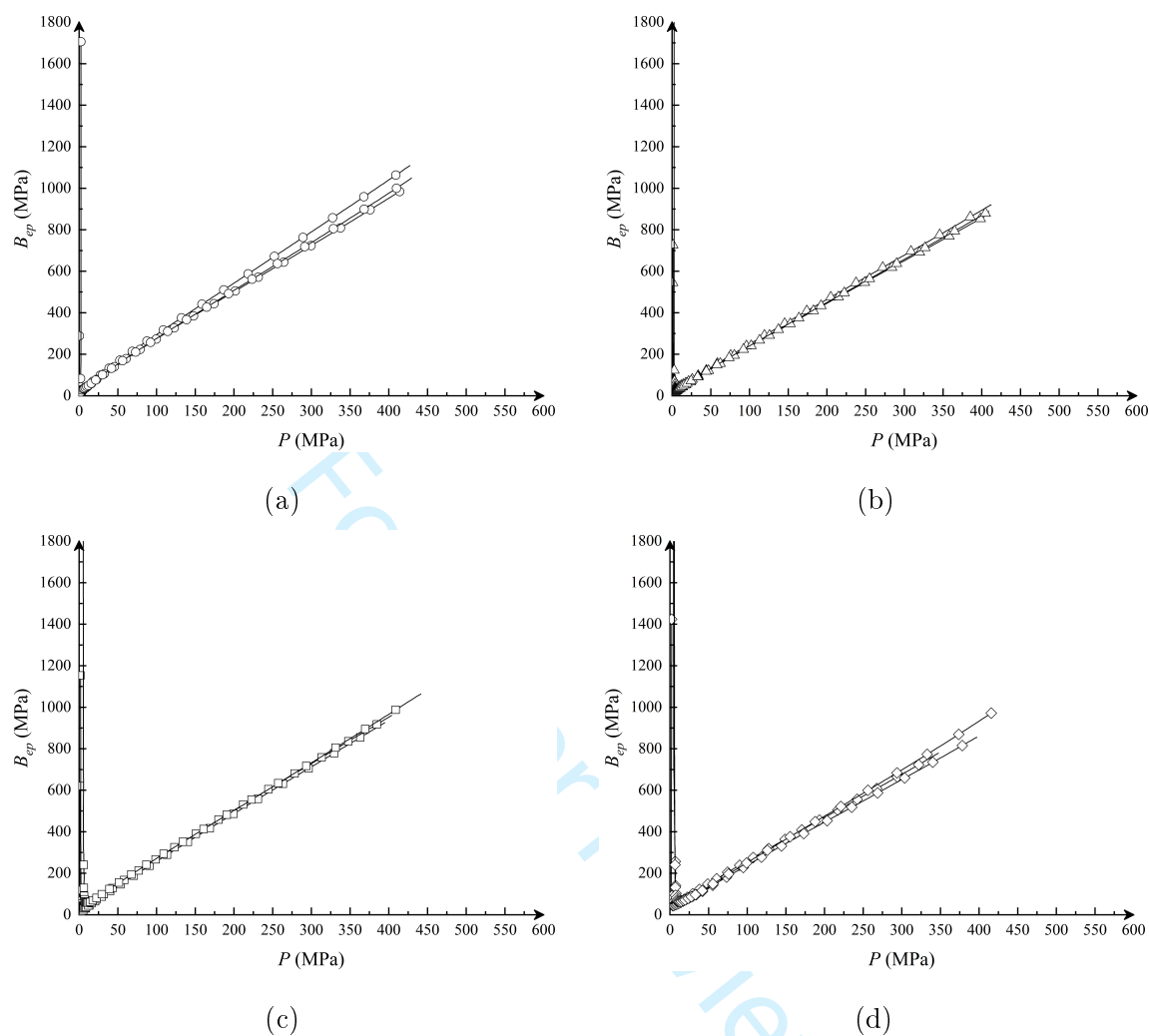


Figure 6: In the figure we see the bulk modulus response of the Al_2O_3 powder as a function of hydro-static pressure. In (a), the bulk modulus response as a function of hydro-static pressure was captured for the range of particles: $170 \pm 63 \mu\text{m}$. In (b), the bulk modulus response as a function of hydro-static pressure was captured for the particle size range: $230 \pm 55 \mu\text{m}$. In position (c) the bulk modulus response as a function of hydro-static pressure was captured for the particle size range: $330 \pm 67 \mu\text{m}$. In position (d), the bulk modulus response as a function of hydro-static pressure was captured for particle size range: $450 \pm 83 \mu\text{m}$.

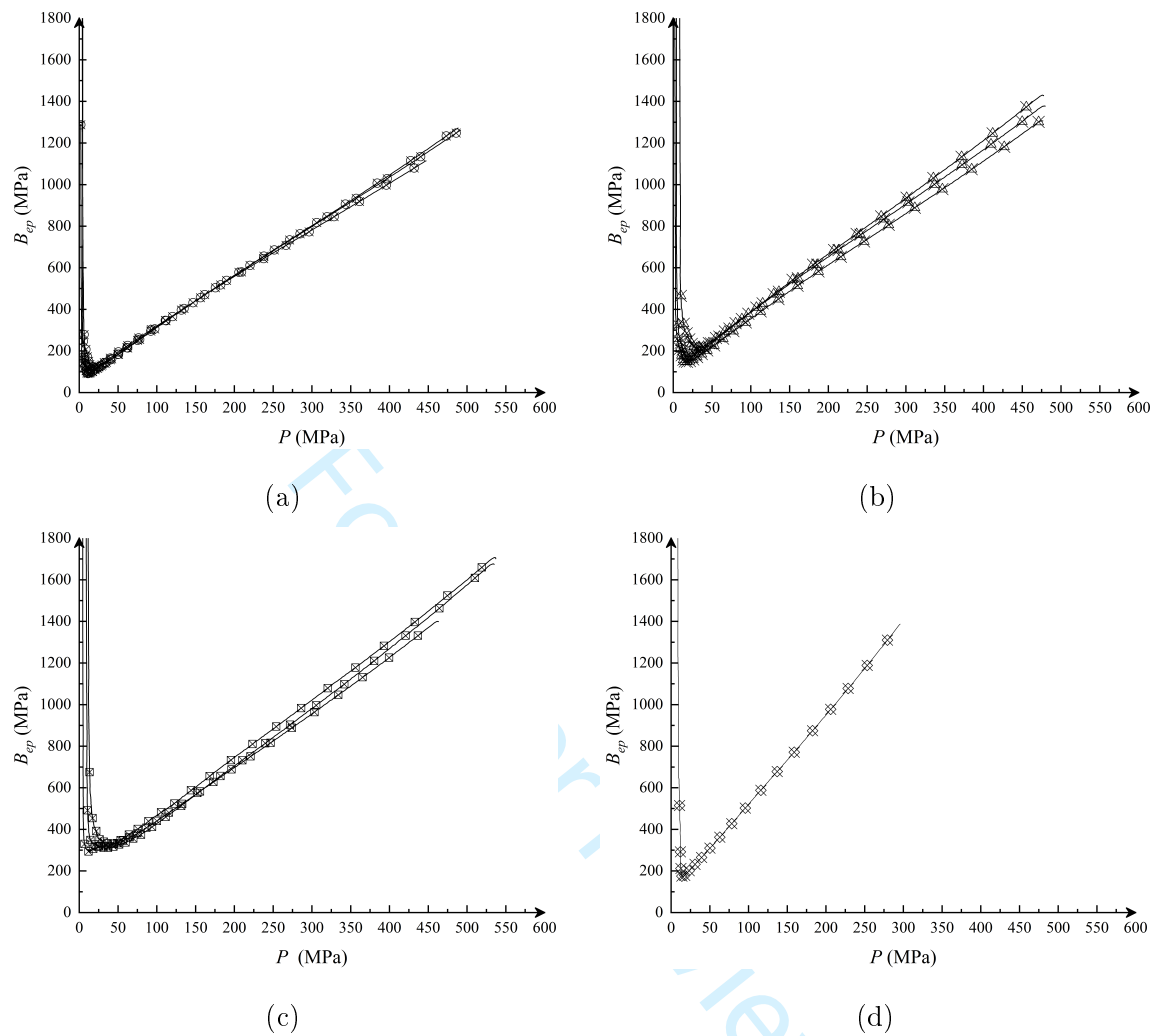


Figure 7: In the figure we see the hydro-static response of granular B_4C . In (a), the bulk modulus response as a function of hydro-static pressure was captured for the range of particles: $170 \pm 40 \mu\text{m}$. In (b), the bulk modulus response as a function of hydro-static pressure was captured for the particle size range: $190 \pm 34 \mu\text{m}$. In position (c) the bulk modulus response as a function of hydro-static pressure was captured for the particle size range: $320 \pm 59 \mu\text{m}$. In position (d), the bulk modulus response as a function of hydro-static pressure was captured for particle size range: $470 \pm 90 \mu\text{m}$.

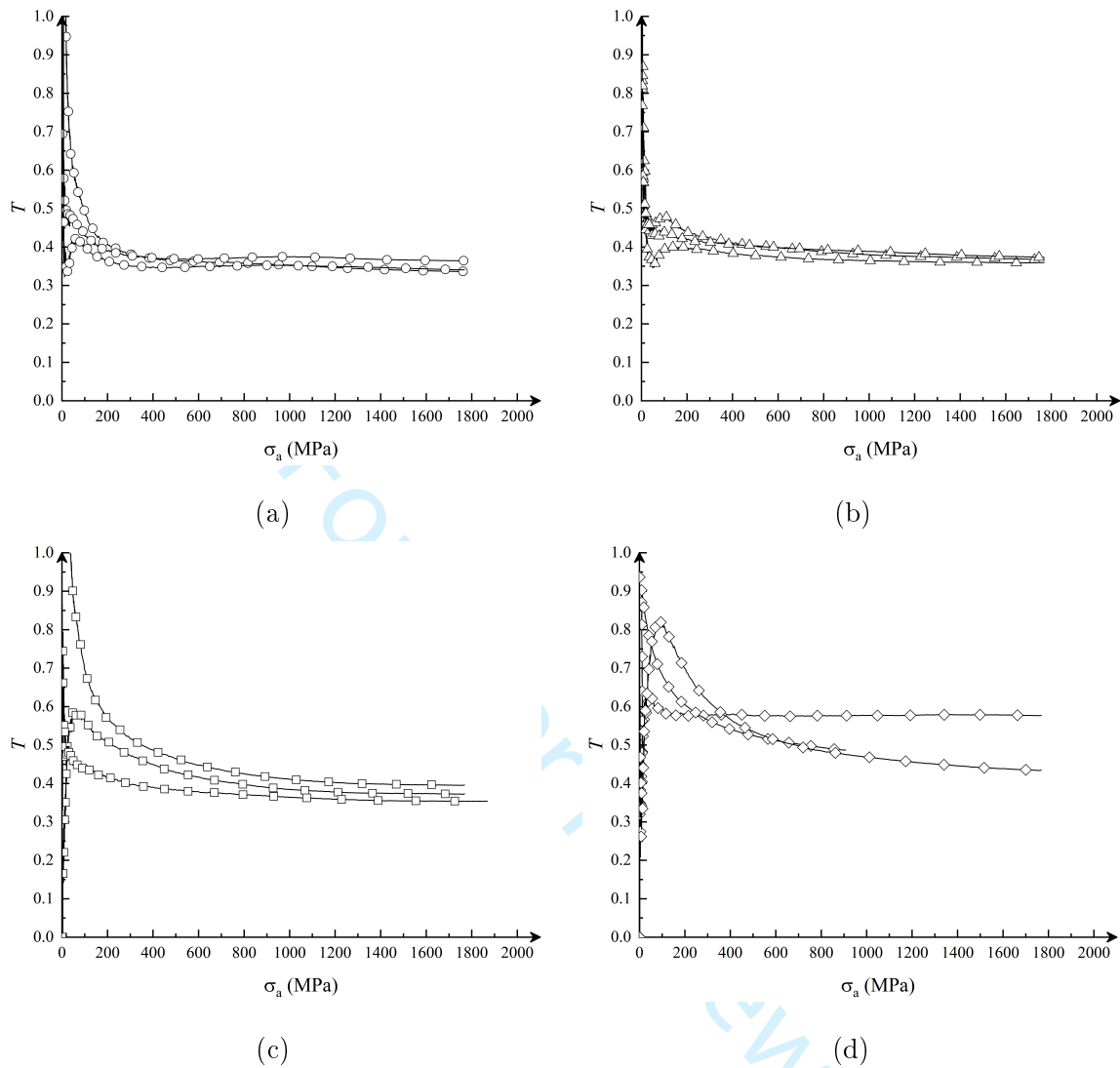


Figure 8: In the figure we see the transmission ratio of the Al_2O_3 powder as a function of applied stress. In position (a), the transmission ratio response as a function of the applied stress was captured for the range of particles: $170 \pm 63 \mu\text{m}$. In position (b), the transmission ratio as a function of applied stress was captured for the particle size range: $230 \pm 55 \mu\text{m}$. In position (c) the transmission ratio was captured for the particle size range: $330 \pm 67 \mu\text{m}$. In position (d), the transmission ratio was captured for particle size range: $450 \pm 83 \mu\text{m}$.

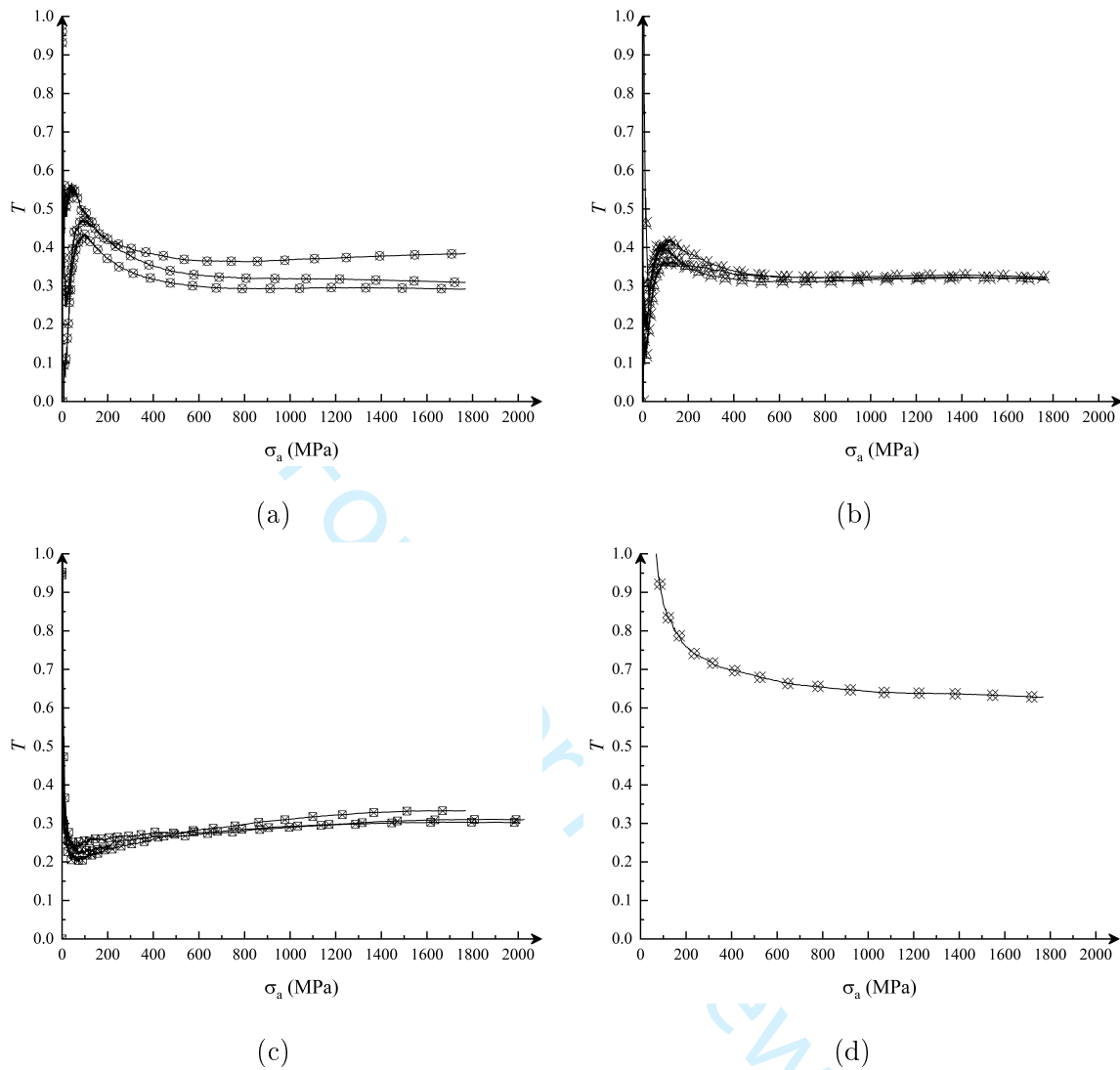


Figure 9: In the figure we see the transmission ratio of the B_4C powder as a function of applied stress. In position (a), the transmission ratio response as a function of the applied stress was captured for the range of particles: $170 \pm 40 \mu\text{m}$. In position (b), the transmission ratio as a function of applied stress was captured for the particle size range: $190 \pm 34 \mu\text{m}$. In position (c) the transmission ratio was captured for the particle size range: $320 \pm 59 \mu\text{m}$. In position (d), the transmission ratio was captured for particle size range: $470 \pm 90 \mu\text{m}$.

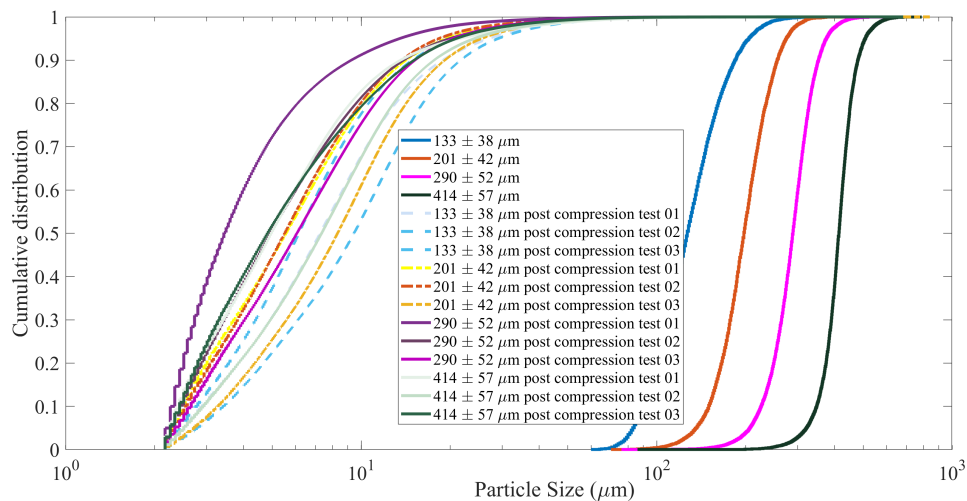


Figure 10: The cumulative distribution of the particles for Al_2O_3 powder for the range of particles: $133 \pm 38 \mu\text{m}$, $201 \pm 42 \mu\text{m}$, $290 \pm 52 \mu\text{m}$, and $414 \pm 57 \mu\text{m}$. Characterization pre-experiment was done on the bulk sample, while post-test characterization was done for each of the three repeated experiments (termed test 01, test 02, test 03).

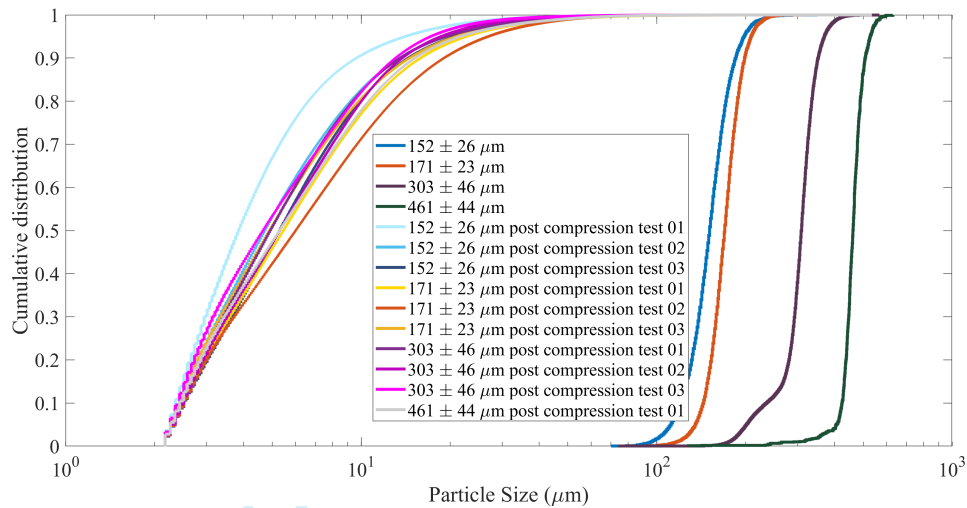


Figure 11: The cumulative distribution of the particles for B₄C powder for the range of particles: 152 ± 26 μm, 171 ± 23 μm, 303 ± 46, and 461 ± 44 μm. Characterization pre-experiment was done on the bulk sample, while post-test characterization was done for each of the three repeated experiments (termed test 01, test 02, test 03).

List of Figures

- 1 SEM images were taken of the Al_2O_3 powder to observe powder morphology before experiments and failure features post-experiment. (a) depicts the Al_2O_3 powder ($170 \pm 63 \mu\text{m}$) before compression. (b) depicts the Al_2O_3 powder ($170 \pm 63 \mu\text{m}$) after compression. Lastly, position (c) depicts the large Al_2O_3 powder ($450 \pm 83 \mu\text{m}$) after the experiment showing the resulting material size and shapes and (d) depicts surface features of the $450 \pm 83 \mu\text{m}$ Al_2O_3 powder.
- 2 SEM images of B_4C were taken to observe the small and large particles, focusing on powder morphology before and after experiment. Position (a) depicts $170 \pm 40 \mu\text{m}$ B_4C powder before compression. Position (b) depict the $320 \pm 59 \mu\text{m}$ particle size showing the overall geometry before compression. Position (c) depict the postmortem $320 \pm 59 \mu\text{m}$ powder visualizing the overall fragment distribution and (d) depicts the surface features post experiment.
- 3 An isometric cross-section view is shown of the compaction apparatus used in compressing Al_2O_3 & B_4C powders to show the different components. The colour in the figure is to distinguish various components that constitute the apparatus.

- 1
2
3
4
5
6
7
8
9
10
11
12
13
14
15
16
17
18
19
20
21
22
23
24
25
26
27
28
29
30
31
32
33
34
35
36
37
38
39
40
41
42
43
44
45
46
47
48
49
50
51
52
53
54
55
56
57
58
59
60
- 4 In the figure we see the hydro-static pressure response of granular Al_2O_3 . In (a), the hydro-static pressure response as a function of porosity was captured for the range of particles $170 \pm 63 \mu\text{m}$. In (b), the hydro-static pressure response as a function of porosity was captured for the particle size range $230 \pm 55 \mu\text{m}$. In position (c) the hydro-static pressure response was captured for the particle size range $330 \pm 67 \mu\text{m}$. In position (d), the hydro-static pressure response was captured for particle size range $450 \pm 83 \mu\text{m}$.
- 5 In the figure we see the hydro-static pressure response of granular B_4C . In (a), the hydro-static pressure response as a function of porosity was captured for the range of particles: $170 \pm 40 \mu\text{m}$. In (b), the hydro-static pressure response as a function of porosity was captured for the particle size range: $190 \pm 34 \mu\text{m}$. In position (c) the hydro-static pressure response was captured for the particle size range: $320 \pm 59 \mu\text{m}$. In position (d), the hydro-static pressure response was captured for particle size range: $470 \pm 90 \mu\text{m}$.
- 6 In the figure we see the bulk modulus response of the Al_2O_3 powder as a function of hydro-static pressure. In (a), the bulk modulus response as a function of hydro-static pressure was captured for the range of particles: $170 \pm 63 \mu\text{m}$. In (b), the bulk modulus response as a function of hydro-static pressure was captured for the particle size range: $230 \pm 55 \mu\text{m}$. In position (c) the bulk modulus response as a function of hydro-static pressure was captured for the particle size range: $330 \pm 67 \mu\text{m}$. In position (d), the bulk modulus response as a function of hydro-static pressure was captured for particle size range: $450 \pm 83 \mu\text{m}$.

- 1
2
3
4
5 7 In the figure we see the hydro-static response of granular B_4C . In (a),
6 the bulk modulus response as a function of hydro-static pressure was
7 captured for the range of particles: $170 \pm 40 \mu\text{m}$. In (b), the bulk
8 modulus response as a function of hydro-static pressure was captured
9 for the particle size range: $190 \pm 34 \mu\text{m}$. In position (c) the bulk
10 modulus response as a function of hydro-static pressure was captured
11 for the particle size range: $320 \pm 59 \mu\text{m}$. In position (d), the bulk
12 modulus response as a function of hydro-static pressure was captured
13 for particle size range: $470 \pm 90 \mu\text{m}$.
- 14
15
16
17
18
19
20
21 8 In the figure we see the transmission ratio of the Al_2O_3 powder as
22 a function of applied stress. In position (a), the transmission ratio
23 response as a function of the applied stress was captured for the range
24 of particles: $170 \pm 63 \mu\text{m}$. In position (b), the transmission ratio as
25 a function of applied stress was captured for the particle size range:
26 $230 \pm 55 \mu\text{m}$. In position (c) the transmission ratio was captured for
27 the particle size range: $330 \pm 67 \mu\text{m}$. In position (d), the transmission
28 ratio was captured for particle size range: $450 \pm 83 \mu\text{m}$.
- 29
30
31
32
33
34
35
36 9 In the figure we see the transmission ratio of the B_4C powder as a
37 function of applied stress. In position (a), the transmission ratio re-
38 sponse as a function of the applied stress was captured for the range
39 of particles: $170 \pm 40 \mu\text{m}$. In position (b), the transmission ratio as
40 a function of applied stress was captured for the particle size range:
41 $190 \pm 34 \mu\text{m}$. In position (c) the transmission ratio was captured for
42 the particle size range: $320 \pm 59 \mu\text{m}$. In position (d), the transmission
43 ratio was captured for particle size range: $470 \pm 90 \mu\text{m}$.
- 44
45
46
47
48
49
50
51
52

- 1
2
3
4
5 10 The cumulative distribution of the particles for Al_2O_3 powder for
6 the range of particles: $133 \pm 38 \mu\text{m}$, $201 \pm 42 \mu\text{m}$, $290 \pm 52 \mu\text{m}$, and
7 $414 \pm 57 \mu\text{m}$. Characterization pre-experiment was done on the bulk
8 sample, while post-test characterization was done for each of the three
9 repeated experiments (termed test 01, test 02, test 03).
10
11
12
13
14 11 The cumulative distribution of the particles for B_4C powder for the
15 range of particles: $152 \pm 26 \mu\text{m}$, $171 \pm 23 \mu\text{m}$, 303 ± 46 , and 461 ± 44
16 μm . Characterization pre-experiment was done on the bulk sample,
17 while post-test characterization was done for each of the three repeated
18 experiments (termed test 01, test 02, test 03).
19
20
21
22
23

24 List of Tables

- 25
26
27 1 Al_2O_3 Powder Characterization: the material span is Δ (unit-less), the
28 tenth percentile D_{10} (μm), the fiftieth percentile D_{50} (μm), ninetieth
29 percentile D_{90} (μm), and the aspect ratio with respect to the width
30 and length, w/l , of the distribution.
31
32
33 2 B_4C Powder Characterization: the material span is Δ (unit-less), the
34 tenth percentile D_{10} (μm), the fiftieth percentile D_{50} (μm), ninetieth
35 percentile D_{90} (μm), and the aspect ratio with respect to the width
36 and length, w/l , of the distribution.
37
38
39 3 Al_2O_3 experiment parameters: mean diameter \bar{O} (μm), mass m (g),
40 initial void volume V_i (mm^3), initial density ρ (kg m^{-3}), final density
41 ρ (kg m^{-3}), initial porosity ϕ_i (%), and final porosity ϕ_f (%).
42
43
44
45
46
47
48
49
50
51
52

- 1
2
3
4
5 4 B₄C experiment parameters: mean diameter \bar{O} (μm), mass m (g), ini-
6 tial void volume V_i (mm^3), initial density ρ (kg m^{-3}), final density ρ
7 (kg m^{-3}), initial porosity ϕ_i (%), and final porosity ϕ_f (%).
8
9
10 5 Systematic uncertainty: propagation of error
11
12
13
14
15
16
17
18
19
20
21
22
23
24
25
26
27
28
29
30
31
32
33
34
35
36
37
38
39
40
41
42
43
44
45
46
47
48
49
50
51
52